Sentinels4Carbon (Sense4Fire)

Sentinel-based fuel, fire and emissions products to constrain the changing role of vegetation fires in the global carbon cycle

ESA Contract Number: 4000134840/21/I-NB

Algorithm Theoretical Baseline Document Version 2.1

(ATBDv2.1)

5 May 2023, Version 2.1

Prepared by:

Matthias Forkel, Christine Wessollek, Daniel Kinalczyk, Christopher Marrs

Technische Universität Dresden, Faculty of Environmental Sciences, Dresden, Germany

Vincent Huijnen, Jos de Laat

Royal Netherlands Meteorological Institute (KNMI), De Bilt, The Netherlands

Niels Andela, Alfred Awotwi

Cardiff University, School of Earth and Environmental Sciences, Cardiff, Wales, UK

Contents

Figures

Tables

Acronyms

AGB	Above ground Biomass
ASCAT	Advanced Scatterometer
ATBD	Algorithm Theoretical Baseline Document
BAAD	Biomass and Allometry Database
BAMT	Burned Area Mapping Tools
BFAST	Breaks for Additive Seasonal and Trend
CC	Combustion Completeness
CWD	Coarse Woody Debris
DFMC	Dead Fuel Moisture Content
DRC	Democratic Republic of Congo
ESA	European Space Agency
EVT	Existing Vegetation Type
FAPAR	Fraction of Absorbed Photosynthetic Active Radiation
FC	Fuel Consumption
F(COVER)	Fractional Cover of Green Vegetation
FL	Fuel Load

FMC	Fuel Moisture Content
FRE	Fire Radiative Energy
FRP	Fire Radiative Power
FWD	Fine Woody Debris
GEDI	Global Ecosystem Dynamics Investigation
GENOUD	Genetic Optimisation Using Derivatives
GFAS	Global Fire Assimilation System
GFED	Global Fire Emission Database
GLAD	Global Land Analysis and Discovery
LAI	Leaf Area Index
LFMC	Live Fuel Moisture Content
NAWFD	North American Wildland Fuel Database
NBR	Normalised Burn Ratio
OLCI	Ocean and Land Colour Instrument
PFT	Plant Functional Type
PRODES	Project for Monitoring Amazon Deforestation
PVR	Product Validation Report
RBR	Requirement Baseline Review
SLA	Specific Leaf Area
SLSTR	Sea and Land Surface Temperature Radiometer
SMAP	Soil Moisture Active Passive
SMOS	Soil Moisture and Ocean Salinity
SWI	Soil Water Index
VIIRS	Visible Infrared Imaging Radiometer Suite
VOD	Vegetation Optical Depth
VODCA	Vegetation Optical Depth Climate Archive
VWC	Vegetation Water Content

1 Introduction

This Algorithm Theoretical Baseline Document (ATBD) describes the methods and required input datasets that are developed within the ESA-funded Sense4Fire project: Sentinel-based fuel, fire and emissions products to constrain the changing role of vegetation fires in the global carbon cycle. The aim of Sense4Fire is to increase the scientific understanding of fire dynamics and their role in the carbon cycle by integrating observations from the Sentinels into new Earth observation products. We understand fire dynamics as all processes that contribute to pre-fire conditions of the land surface (i.e. fuel loads and fuel moisture), fire behaviour (fire ignitions, spread, speed, size, burned area, thermal emissions and radiative power), combustion and production of fire emissions (combustion completeness, combustion efficiency, biomass burning and composition of emissions) and the effect of fire emissions on atmospheric composition (injection height, smoke plumes, atmospheric gas composition, aerosols).

This second version of the ATBD (ATBDv2.1) builds on the state of the art and requirement baseline that was reviewed and summarised in the Requirement Baseline Review (RBR) document and the Database Description from 31.10.2021 and is an update of the first version of the ATBD (ATBDv1.1) from 11.11.2022. Based on the objectives outlined in the RBR, we describe here the methods that are used to develop and generate novel and advanced geo-information products to quantify the spatial-temporal variability in fuel conditions, fire behaviour and fire emission estimates. These estimates are mainly based on observations from Sentinel-3 and -5p and supported by data from Sentinel-1 and -2 and additional European Earth observation datasets. ATBDv2 is accompanied with the second version of the **Product Validation Report (PVRv2.1)** (Forkel et al., 2022), which presents the approach to calibrate and validate results.

This document first provides an overview of the study regions and test areas (Chapter 2) and then describes the three different approaches that are developed in Sense4Fire to estimate fire emissions. Each approach aims to estimate fire emissions by considering properties of individual fires:

- **GFA-S4F** is based on the Global Fire Atlas (GFA) algorithm (Andela et al., 2019, 2022) and uses observations of active fires from the VIIRS and Sentinel-3 SLSTR instruments with a new fire type map to estimate fire emissions (Chapter 3).
- **TUD-S4F** is a new data-model fusion approach that combines several datasets from Sentinel-3 and other Earth observation products to estimate fuel loads, fuel moisture, fuel consumption, and fire emissions. (Chapter 4)
- **KNMI-S5p** is based on observation from Sentinel-5p, whereby fire emissions of CO and NOx are estimated using a top-down approach (Chapter 5).

2 Spatial and temporal domain and study areas

2.1 Study regions and test areas

Our study domain includes three RECCAP-2 regions: Brazil, Russia, and Southern Africa. Within these study regions, we have apply the approaches to three smaller test areas that include a range of representative land cover and fire types (Table 1). The test areas include a transect from frequently burning tropical forests to savannah in Brazil, an area with small agricultural and large savannah fires in southern hemisphere Africa, and a boreal forest to tundra region in Eastern Siberia. In the Amazon/Brazil and southern Africa, we additionally applied the approaches to a larger study region.

Table 1: Overview about the study regions (large) and test areas (small).

Study region or test area	East/West extent	North/South extent
Amazon study region	40°W - 80°W	25°S - 10°N
Amazon test area	50°W - 55°W	9°S - 14°S
Southern Africa study region	10°E - 30°E	5°S - 25°S
Southern Africa test area	23°E - 28°E	11°S - 16°S
Siberia test area	132°E - 138°E	60°N - 71°N

For initial analysis we have, for each test area, identified the fire season during 2020 for atmospheric modelling purposes. Fire activity can vary considerably from year-to-year and 2020 was found to be of particular interest for the selected regions (e.g., extensive drought driven understorey fires in Brazil, and large forest fires in Eastern Russia).

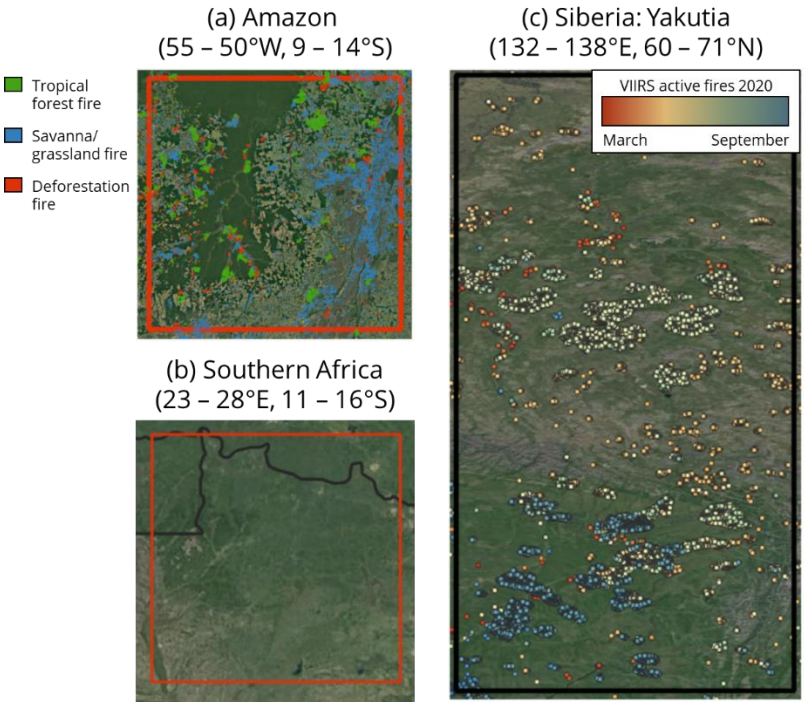

Figure 1: Detailed maps of the test areas. In the Amazon region in (a) fire types are mapped based on VIIRS active fire observations using a recently developed approach by Andela et al. (2022). No active fires are shown in the southern Africa test site (b) because a large proportion of this landscape is burned annually resulting in a large amount of active fire detections which cannot be interpreted at this scale.

2.2 Amazon

The first test area is located in the Brazilian Amazon, where decades of expansion of the land use frontier into tropical forests has led to increasing concerns about forest conservation. Until recently the role of fire in the process of tropical forest degradation remained unclear because satellites can detect fires, but not their type nor underlying causes. Our selected study region (Figure 1a), including the Xingu protected areas, includes a mix of fire types relevant for forest degradation. Firstly, the region includes large areas of active deforestation, followed by fires to remove residual organic material and prepare fields for agriculture or grazing. Secondly, it is a region that is particularly sensitive to forest fires during drought years, such as 2020. Finally, the region includes extensive and frequently burnt natural savannah, the third important regional fire type. Initial results indicate a good capability to separate these regional fire types (Figure 1a and see PVRv2).

2.3 Southern Africa

The second test area, located in the southern Africa study region, represents a large moisture gradient, from the more arid savannahs to dense woodlands (Figure 1b). Therefore, this region includes both large grassland fires and woodland degradation fires towards the end of the dry season. In addition, the region also highlights the strong human signature in fire occurrence, including many small agricultural burns and higher intensity burns associated with land clearing. Identifying these different fire types and

their temporal contributions to burned area and fuel consumption will enable us to use top-down emissions modelling to constrain emissions factors, combustion efficiency and total carbon emissions.

2.4 Siberia/Yakutia

The third test area, located in eastern Siberia/Yakutia in Russia, covers an environmental gradient ranging from open Tundra landscapes in the north, towards increasingly dense Taiga forests in the south (Figure 1c). Fuel loads and properties such as drainage conditions and tree species composition are important controls on fire emissions in boreal forests (Walker et al., 2020). Recently, there has been an increased interest in tundra burning because of subsequent acceleration of permafrost melt and subsequent increase in shrubs and trees. In contrast, regional warming has intensified the burning of Taiga forests, with unknown outcomes for forest density, carbon storage and post-fire recruitment and recovery (Barrett et al., 2020; Shvetsov et al., 2019). Here we aim to separate crown from ground fires, to better understand wildfire emissions and the long-term consequence for above ground biomass. Our study is the first to identify these regionally important fire types and constrain their emissions and therefore provides an important step forward for our understanding of ecosystem change.

3 GFA-S4F: Fire emissions from fire types

3.1 Theoretical baseline

To date, global fire emissions datasets (e.g., GFED, GFAS) have focused on gridded estimates of burned area or active fire detections with associated fire radiative power to derive total carbon and trace gas emissions. Nevertheless, fuel consumption and emissions factors directly depend on “what” is burning (e.g., deforestation or grassland fires), and at what intensity. Here we develop an object-based approach to estimate global fire emissions. The approach builds upon the recently developed Global Fire Atlas (Andela et al., 2019) and “Amazon dashboard” (Andela et al., 2022), that tracks individual fires and their behaviour (e.g., perimeters, speed, duration, radiative power) based on near real time detection of active fires from the VIIRS sensors on-board NOAA20 and Suomi-NPP. Here we expand on these approaches by (1) including night-time active fire detections from Sentinel-3 SLSTR instruments to map fire perimeters (Section 3.3), (2) combine land cover information with 10-m resolution Sentinel-2 data to identify regionally relevant fire types (Section 3.4), and (3) use Sentinel-2 surface reflectance data to constrain burned area associated with each fire object (Section 3.5). Section 3.2 provides a short overview of datasets used.

3.2 Input data

This section provides a short overview of the dataset used (Table 2). Active fire detections from the VIIRS instruments onboard S-NPP and NOAA20 and SLSTR onboard Sentinel-3A/B are used to track individual fire events and characterize their behaviour. Because active fire detections provide only information about actively burning fires at cloud free satellite overpass, we use surface reflectance data and an existing burned area products from Sentinel-2 and MODIS to estimate the burned area associated with each fire event. Finally, we use a variety of datasets to classify fires into different fire types. Full detail on the use of these datasets is provided in Section 3.3 (Fire Event Monitoring), 3.4 (Fire type classification) and 3.4 (Burned area mapping).

Table 2: Overview of datasets used for fire tracking, burned area mapping and fire type identification. A detailed description of each dataset is provided in the corresponding report (D2.2 Database Description).

Variables	Dataset (Sensor)	Spatial resolution and coverage	Temporal resolution and coverage
Fire event monitoring			
Active fire detections	Sentinel-3 SLSTR	1 km, all domains	Night-time (10 pm) daily for 2020
Active fire detections	S-NPP and NOAA20 VIIRS	375 m, all domains	1:30 am/pm daily for 2020
Burned area mapping			
Surface reflectance	Sentinel-2	20 m, sample across all domains	5-daily 2019-2020
FireCCI burned area (SFD11)	Sentinel-2	20 m, Africa	5-daily 2016, 2019
MCD64A1 burned area	MODIS	500 m, Brazil	Daily, 2019
Fire type classification			
Surface reflectance, visual interpretation of fire type	Sentinel-2	10 m, fire sample	Pre- and post-fire image pairs for 2020
Land cover	ESA Worldcover V2	10 m, all domains	2021
Deforestation	PRODES	30 m, Brazil	Annual, 2015-2020
Tree cover	Global Forest Change dataset	30 m, Brazil	Annual, 2020
Biomass	Avitabile	30 m, Brazil	

3.3 Fire event monitoring

The combination of Sentinel-3 and VIIRS active fire detections provides a point cloud of active fire detections and associated detection dates at a daily temporal resolution. Here we cluster these active fire detections into fire events based on the Fire Atlas algorithm (Andela et al., 2019). The Global Fire Atlas algorithm was initially applied to the MCD64A1 collection 6 burned area product, a daily estimate of global burned area at 500 m resolution (Giglio et al., 2018). However, burned area data have two important limitations compared to active fire detections for the development of an algorithm to track fires and associated emissions. First, burned area data are not available in near-real time, as burned area algorithms rely on time series of data before and after the fire, leading to a typical two to three-month delay in the production of global products. Second, coarse resolution (e.g., 500 m) satellite observations are often unable to accurately map the burned area associated with small fire types or low-intensity forest fires burning beneath a dense forest canopy (Morton et al., 2011). Previous studies have demonstrated that active fire data can provide a robust estimate of burned area in forested ecosystems

based on a persistent thermal signal within each larger grid cell from the slow spread rates and residual smouldering (Veraverbeke et al., 2014; Oliva and Schroeder, 2015).

To map individual fire perimeters from Sentinel-3 and VIIRS active fire detections, we first gridded active fire detections at a 0.005° (~550 m) resolution based on the centre of each fire pixel (Figure 2). We selected this spatial resolution to accommodate typical forest fire spread rates of 300 to 500 m day^{-1} and reduce potential effects of geolocation error from the VIIRS Sensor. The 0.005° (~550 m) degree spatial resolution is finer than the 1-km resolution of Sentinel 3 but only about 18% of active fire detections originated from Sentinel-3, and hence we optimized the resolution primarily based on VIIRS. Nevertheless, in addition to information about fire location, the Sentinel-3 data provide useful context on fire behaviour and energy release.

To prepare the data for the Fire Atlas algorithm, we select the earliest active fire detection within each 550 m grid cell (Figure 2). Following the Global Fire Atlas approach, we then apply a spatial filter to remove inconsistencies in the estimated burn date within each fire to identify the ignition location (Andela et al., 2019). Inconsistencies can originate from gaps in the observation record, e.g., due to cloud cover. An additional threshold is required to separate adjacent fires that burned at different times during the fire season. This threshold sets the maximum number of days for a fire to spread into an adjacent grid cell; here, we set this threshold as ≤5 days after the last active fire detection within any given 550 m grid cell. For example, in Figure 2c and Figure 2d, a deforestation fire in an adjacent field burned into the understorey of neighbouring forest area, resulting in fire detections adjacent to our example fire on day 220, eight days before the example fire was ignited. In this case, the algorithm successfully classified these as two separate fire events despite their spatial proximity. In contrast to forest fires, savannah and grassland fires typically spread several kilometres per day, resulting in artificial fragmentation of individual events in our finer 550 m grid. We therefore use land cover data to distinguish grassland from forest fires (Section 3.4) and develop a burned area scaling factor to estimate associated burned areas for each fire type.

Thermal anomalies detected from space are most often fires, but these products also capture other features that are hotter than their surroundings such as volcanoes, gas flares, and industrial activity (Giglio et al., 2016; Schroeder et al., 2014). To remove the influence of static sources on our analysis, we exclude fire events containing 550 m grid cells with more than 20 active fire detections in at least three out of seven historic fire years (2013 – 2019) based on the VIIRS sensor onboard Suomi-NPP. On the other hand, clouds or dense smoke may reduce the ability of the VIIRS instruments to detect active fires. Though this will affect the absolute numbers of active fire detections on any given day, the persistent (multi-day) fire signal within each larger grid cell in this analysis mitigates the influence of unobserved fire activity on the estimated extent of each fire. The combination of both Sentinel-3 and VIIRS instruments also reduces the effect of cloud cover or smoke on daily fire detections because observations are several hours apart. Therefore, the active fire data in this study are not corrected for cloud cover, since

statistical models used in other studies to account for cloud cover cannot be easily attributed to specific fire events (e.g., Kaiser et al., 2012).

Fire radiative energy (FRE, MJ/m²) of a single fire was derived from fire radiative power (FRP, MW/sec) from the Sentinel-3 and VIIRS observations by averaging all FRP values of a single fire, and multiplying the average with fire duration (i.e. MJ/m² = (MW/sec * 86400 sec * number of burning days) / grid cell area).

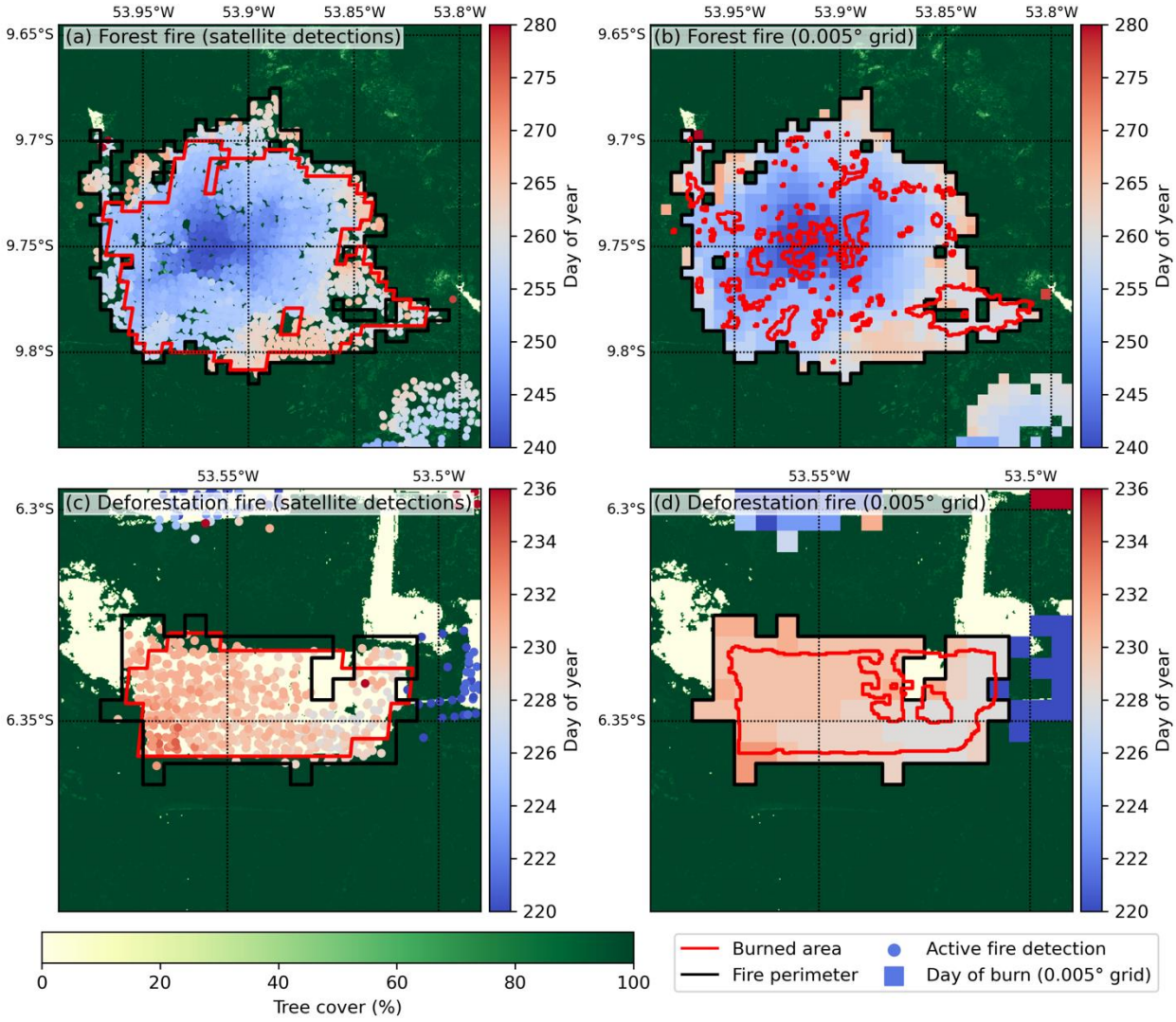

Figure 2: Example of the spatial and temporal evolution of SLSTR and VIIRS active fire detections for Amazon deforestation and forest fires provides an estimate of daily burned area needed for the Global Fire Atlas algorithm. Day of active fire detections (circles) from both SLSTR and VIIRS instruments for (a) a large forest fire and (c) a deforestation fire in Brazil. Panels (b) and (d) show the estimated daily fire progression on a 0.005° (~550 m) grid. The background depicts fractional tree cover (Hansen et al., 2013). Black lines indicate the fire perimeters derived from active fire detections and red lines show the corresponding burned area estimates from the MCD64A1 C6 product (Giglio et al., 2018) in (a) and (c) and Landsat-derived burned area estimates from MapBiomas in (b) and (d).

3.4 Fire type classification

Clustering active fire detections into larger objects provides unique opportunities for the characterisation of fire types, a key parameter related to combustion completeness and

emissions factors. The focus of our algorithm is on carbon losses, and hence we use a straightforward classification of fire types for open cover types, like croplands, grasslands or savannah based on the WorldCover product. For forested systems we provide a more detailed assessment of fire types based on the identification of relevant fire types using Sentinel-2 pre- and post-fire changes in surface reflectance data and expected ecosystem impacts. For example, for the Brazilian study region, we separate three fire types in forested systems: (1) forest fires, (2) deforestation fires, and (3) small clearing and agricultural fires. Forest fires in the boreal region are divided in ground and crown fires, and in Africa we separate those fires associated with woodland degradation from fires burning primarily grasses.

Table 3: Fire types by study region. Forested and non-forested lands were separated based on a simple tree-cover threshold (50%) within the fire-affected area.

Fire type	Study region	Tree cover fraction (%)
Evergreen broadleaf forest fires	Brazil	≥50%
Deforestation fires	Brazil	≥50%
Small clearing and agricultural fires	Brazil	≥50%
Boreal forest ground fires	Russia	≥50%
Boreal forest crown fires	Russia	≥50%
Woodland fires	Africa	≥50%
Cropland burning	Brazil, Africa, Russia	<50%
Savannah and grassland fires	Brazil, Africa, Russia	<50%

Savannah and grassland fires are separated from cropland fires using the WorldCover data product. The remaining fire types all occur in landscapes with ≥ 50% tree cover, and therefore cannot be separated based on land cover data alone. We use training datasets to develop multivariate classification approaches to separate forest fire types. Below we provide a detailed description of the methodology to differentiate the three relevant forest fire types for Brazil, followed by a discussion of the separation of fire types in Russia and Africa.

3.4.1 Fire types for Brazil

We combine attributes of individual fire events derived from the Global Fire Atlas algorithm with existing land cover and land use change information to classify each fire as a specific type. For the Brazil study region, we separate three forest fire types (≥ 50% tree cover): (*i*) deforestation fires, (*ii*) forest fires, (*iii*) small clearing and agricultural fires, and two non-forest fire types (< 50% tree cover), (*iv*) savannah and grassland fires and (*v*) cropland fires.

Selection of training data

To explore the relationship between historic deforestation in the Brazilian Amazon and associated fire activity we use deforestation data from the Project for Monitoring Amazon Deforestation (PRODES) (http://terrabrasilis.dpi.inpe.br/en/home-page/, accessed March 20, 2020.) from the Brazilian National Institute for Space Research (National Institute of

Space Research (INPE). We find elevated fire activity up to five years after the year in which deforestation was initially mapped, based on the repeated use of fire to remove woody debris after initial clearing. Based on this finding, all individual fire events identified by our algorithm with ≥25% of 550 m grid cells associated with historic deforestation (e.g., 2015 – 2019 for the year 2020) are classified as deforestation fires (Figure 3). In addition to evidence for multiple years of fire activity after the year of deforestation, historic deforestation data also provide a strong indicator of active deforestation frontiers, and hence the likelihood of new deforestation and associated fires in 2020. We therefore use this threshold of ≥25% overlap with historic deforestation to create a dataset of 12,039 deforestation fire events to identify their characteristics for model training purposes.

Deforestation and forest fires are particularly challenging to separate, since both fire types may exhibit similar patterns of persistent burning across large, forested areas. We therefore manually selected 77 forest fires across both the Amazon biome and the larger study region, tropical southern hemisphere South America (0-25°S), to identify unique characteristics of this fire type. We select only large forest fires to train the classification for two primary reasons. First, contiguous areas of recent deforestation typically do not exceed 50 km^2, while large forest fires can easily exceed 100 km^2. Second, large forest fires typically develop circular patterns of fire progression based on well-developed fire fronts (Figure 2) that can be easily identified through visual interpretation in standard GIS software. For all selected forest fires in the Brazilian Amazon, less than 5% of 550 m grid cells within each larger understorey fire event contained historic deforestation based on PRODES data.

Fire type classification: identifying thresholds of fire type characteristics

We use three types of information about each individual fire event to identify fire types and assign confidence intervals (Figure 3). First, we use data on land cover and a pan-tropical biomass map. In addition, we include annual layers of fractional tree cover and historic deforestation (This section provides a short overview of the dataset used (Table 2). Active fire detections from the VIIRS instruments onboard S-NPP and NOAA20 and SLSTR onboard Sentinel-3A/B are used to track individual fire events and characterize their behaviour. Because active fire detections provide only information about actively burning fires at cloud free satellite overpass, we use surface reflectance data and an existing burned area products from Sentinel-2 and MODIS to estimate the burned area associated with each fire event. Finally, we use a variety of datasets to classify fires into different fire types. Full detail on the use of these datasets is provided in Section 3.3 (Fire Event Monitoring), 3.4 (Fire type classification) and 3.4 (Burned area mapping).

Table 2). To accommodate delayed effects of tree cover losses on fire, we use estimated forest cover in 2015 to separate savannah from forest fire types, calculated based on the difference between the 2000 fractional tree cover map and 2000 – 2014 tree cover losses from the Global Forest Change dataset at 30 m resolution (Hansen et al., 2013). Historic deforestation (2015 – 2019) is estimated based on 30 m resolution PRODES data available for Brazil (National Institute of Space Research (INPE), PRODES deforestation. http://terrabrasilis.dpi.inpe.br/en/home-page/, accessed March 20, 2020.). We use a pan-

tropical biomass map at 1 km resolution (Avitabile et al., 2016), a product developed from the fusion of two existing biomass maps (Saatchi et al., 2011; Baccini et al., 2012) with additional biomass training data. We combined these data with grid cell level fire characteristics, such as fire persistence and fire radiative power (FRP), and multi-day metrics of fire events such as fire size and total fire detections (Figure 3 and Figure 4). Gridded metrics, like fire persistence (calculated for each 550 m grid cell), are averaged across all grid cells within each fire event, while metrics per fire event, like FRP, are based on equal weight of all satellite fire detections within the fire perimeter. Together, these metrics provide a robust path to classifying fire events by fire type.

Deforestation fires are identified based on historic maps of deforestation and differences in fire behaviour compared to other fire types (Figure 3). Fires containing ≥25% of grid cells with overlapping historic PRODES deforestation during 2015 – 2019 are classified as deforestation fires with high confidence and used to characterise typical deforestation fire behaviour (Figure 4). For all other large fires (>5 fire detections and persistence >1) with ≥50% forest cover, we develop a multivariate approach to separate fire activity from deforestation and forest fire events. Based on the subset of reference fires, we select five indicators of fire behaviour to separate deforestation from forest fires (Figure 3 and Figure 4). In addition, we use a threshold of 120 t ha^{-1} biomass to select between metrics of fire behaviour for forest fires in moist versus dry forest types. In high-biomass Amazon forests, deforestation fires consistently have higher FRP than forest fires, allowing for detection of deforestation fires with high confidence. In lower-biomass forests, typical of drier regions, forest fire behaviour is more similar to savannah fires, with higher average FRP, lower fire persistence (based on faster spread), and a pronounced diurnal cycle resulting in a larger fraction of daytime fire detections.

In low biomass forest systems, deforestation fires are therefore not easily separable from forest fires using fire radiative power. Instead, high confidence deforestation fires are distinguished based on higher fire persistence. Deforestation fires are also typically small compared to forest fires, and we therefore included fire size as an additional indicator of fire type. Fires smaller than 40 km^2 are more likely to be associated with deforestation, whereas fires larger than 100 km^2 are classified as high confidence forest fires. For those fires that cannot be directly classified as either deforestation or forest fire based on these primary indicators, we combine all five metrics to estimate the fire type with three different confidence levels. For each indicator we set a threshold suggesting either deforestation or forest fire activity, if all five metrics indicated deforestation, we assign five points resulting in a high-confidence deforestation fire. At the other extreme, if all five metrics indicate a forest fire, the total of points would be zero, resulting in high-confidence forest fire (see grey box in Figure 3).

Small fires for clearing and agricultural management are identified based on the small total number of active fire detections (≤ 5) and low fire persistence (one day), consistent with fast-spreading fires in herbaceous or other low-biomass fuel loads or short duration. Improved geolocation of the VIIRS 375 m active fire data enables a more robust

combination of fire location with land cover data to rapidly identify fires burning in open cover types. Finally, we use fractional tree cover data to assign all fires with a majority of fire-affected area in landscapes with <50% tree cover to savannah fires and cropland fires based on the dominant land cover type from WorldCover within the fire perimeters. All fire type estimates are based on daily per-fire averages, such that a fire that started in a savannah adjacent to forest cover is classified as a forest fire once the average tree cover across all grid cells within the perimeter exceeds 50%.

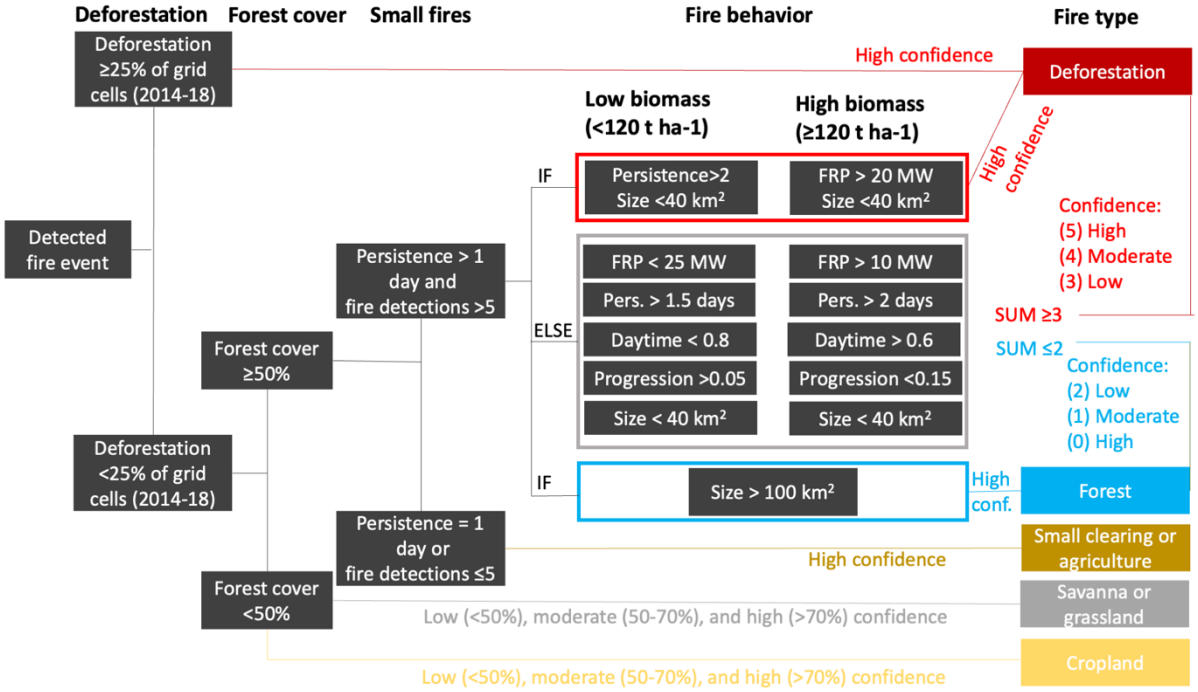

Figure 3: Flow diagram of the fire type classification system and confidence level assessment for Brazil. Fires are separated into deforestation, forest, small clearing and agricultural, savannah and grassland, and cropland fires using metrics of fire behaviour and land cover information. The initial separation between high-confidence deforestation fires and non-forest fires uses historic deforestation data (2014 – 2018), fractional tree cover (2014) and land cover information. For all forest fire types, with ⩾50% tree cover, we first isolate small clearing and agricultural fires based on low fire persistence and number of fire detections. To further separate deforestation fires from forest fires we use a separate classification for low biomass (left column, <120 t ha^{-1}) and high biomass (right column, ⩾120 t ha^{-1}) systems based on observed differences in fire behaviour in moist and dry forests, respectively (see Figure. 5).

Table 4: Variables used to identify fire types in the Amazon region. All variables are based on the aggregate or average for each fire event.

Variable	Explanation	Units
Deforestation	Fraction of 550 m grid cells with historic deforestation (past 5 years) within the fire perimeter	%
Forest cover	Average tree cover fraction within perimeter (corrected for historic forest loss)	%
Fire detections	Total active fire detections from SLSTR and VIIRS within fire perimeter	-

Persistence	Average fire persistence (days with fire activity in each grid cell) across 550 m grid cells within fire perimeter	days
Size	Fire size	km^2
Fire radiative power (FRP)	Average fire radiative power for all active fire detections within the fire perimeter	MW
Daytime fraction	Fraction of 1:30 pm detections for all fire detections within the fire perimeter (VIIRS only)	0 to 1 (no units)
Progression	Average fire progression fraction across 550 m grid cells within perimeter	0 to 1 (no units)

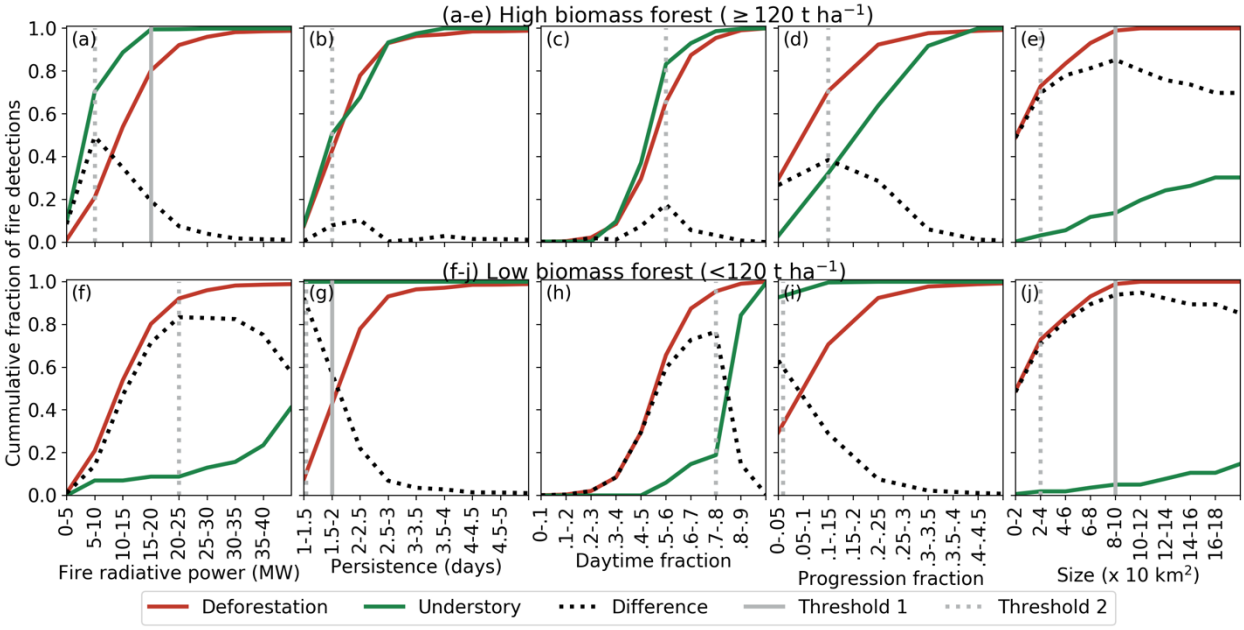

Figure 4: Five fire behaviour metrics distinguish deforestation from forest fires in Brazil. (a) Fire radiative power is a measure of instantaneous energy release by a fire. (b) Persistence indicates the number of days a fire was active within any given 550 m grid cell. (c) The daytime fraction shows the ratio of 1:30 PM to 1:30 AM active fire detections from VIIRS, indicative of the magnitude of diurnal variability in fire behaviour for multi-day fires. (d) The progression fraction is the fraction of FRP observed on the second day of the fire compared to the sum of observed FRP on the first two days. Gradual fire spread, typical of slow-moving forest fires in high biomass ecosystems, results in more equal FRP on days one and two, while the progression from flaming to smouldering combustion in deforestation fires results in a rapid decline in FRP. (e) Fire event size. Figures (f-j) are like (a-e) but for fires in forested ecosystems with average biomass below 120 t ha^{-1}. Threshold 1 (solid grey lines) indicates high confidence classification thresholds shown in Figure 4 and threshold 2 (dashed grey lines) indicate the five thresholds used in the multivariate decision scheme shown in Figure 4 to assign fire type and associated confidence levels.

3.4.2 Fire types for Russia

For Russia, we identify four different fire types, including cropland, grassland and two types of forest fires. Initially, fires are separated into cropland, grassland and forest fires. If tree cover fraction (WorldCover V2) within the fire perimeter exceeded 50% a fire was classified as forest fire. Any fire not meeting this criterion, was classified as cropland or grassland fire, depending on the dominant land cover type within the fire perimeter.

As a second step, we developed an approach to separate forest fire types based on fire behaviour and a training dataset of pre- and post-fire Sentinel-2 images. Wildfires in

boreal Asia are unique in terms of their duration, a single wildfire can burn for months including various seasons. Moreover, the landscape is highly heterogeneous in terms of vegetation type and moisture conditions leading to a range of burning conditions and fire impacts for most fires. Here we use detailed land cover information to capture most of this variability, but in addition we aim at understanding the long-term impacts of fire on forests. Within the test area, we investigate the extent to which forests are impacted by fire by separating ground from crown fires (Figure 5). We use a manually selected sample (about 100 for each type) of 'end members' (clearly identifiable examples) of relevant forest fire types to train our model and to assess accuracy (see PVRv2). Since our aim is to develop an approach that can identify fire types in near-real time, our classification is based on fire characteristics along with recent land cover information but does not include changes in surface reflectance following the fire (e.g., dNBR etc.). Nevertheless, surface reflectance data at 10-20 m from Sentinel 2 provide a wealth of information about the underlying processes that can be used for training and validation purposes.

Figure 5: Two forested sites before (September 2019; top panels) and after (September 2020; bottom panels) a large fire that burned both areas in 2020.The left subplots faced greater canopy damage compared to the forested areas in the right subplots. Note that each site includes a mix of forested and open landscapes. The red dots indicate locations of active fire detections.

3.4.3 Fire types for Africa

For the African study region, we separated three fire types based on the WorldCover V2 dataset. If tree cover fraction (WorldCover V2) within the fire perimeter exceeded 50% a fire was classified as woodland fire. Any fire not meeting this criterion, was classified as cropland or grassland and savannah fire, depending on the dominant land cover type within the fire perimeter.

3.5 Burned area mapping, scaling and emissions

We combine the fire objects (Section 3.3) and classification (Section 3.4) with estimates of burned area (m^2) and fuel consumption (g m^{-2}) to derive estimates of total dry matter burned (g) and carbon emissions per fire. For large and high fuel-load fires, our polygons compare well to estimated burned area, but for smaller fire types and fast-moving grassland and savannah fires scaling is required. We therefore first translate fire perimeters derived here to estimates of area burned using scaling factors.

3.5.1 Burned area mapping

To scale and validate initial burned area estimates from the Fire Atlas perimeters, we require consistent high quality burned area data for all three study regions (Brazil, Russia, and southern Africa). Here we used the Sentinel-2 based Burned Area Mapping Tools (BAMT) developed by Roteta et al. (2021) for Google Earth Engine to generate a sample of high quality burned area. Initially we used the FireCCI Sentinel-2 burned area product (Africa) for 2019 to identify a training strategy for the BAMT algorithm. By using FireCCI Sentinel-2 burned area as reference, we find optimal performance when the BAMT algorithm is provided with training data using a mix of 15 training samples with moderate (about 5) to high (about 10) dNBR derived from Sentinel-2. This resulted in accurate (typical accuracy about 90%) burned area estimates as compared to the FireCCI Sentinel-2 burned area product in the absence of cloud cover.

3.5.2 Burned area scaling factors

For forest fires in both tropical and boreal regions we find strong correspondence between the fire perimeters mapped by our approach and corresponding burned area (see PVRv2 and Andela et al., 2022) and hence we directly use our estimates of fire perimeters as estimate of burn extent (a scaling factor of one). Nevertheless, for open cover types, our burned area estimates contain significant bias and scaling factors are required.

As a first step we therefore require burned area estimates for each fire type for training purposes. We used the BAMT approach to map burned area in the African and Russian test areas. In addition, we use the MCD64A1 burned area product to scale burned area from grassland and savannah and deforestation fires in South America (Fig. 6). For each continuous cluster of burned area we determine the fire type based on the overlap with fire events from clustering of active fire detections and use the dominant fire type within each cluster (largest overlapping area). For non-forested fire types, where less overlap with active fires is expected, we use the dominant land cover from WorldCover to classify the fire types (savannah and grassland and cropland fires) of any remaining burned area. A small fraction of burned area (<1%) and fire polygons in forested regions could not be matched and are excluded for scaling purposes. Spatially explicit scaling factors are derived for the South American study region and the African, and Russian test areas using

the ratio of burned area derived from the reference data and the fire polygons derived here (e.g., see Figure 6).

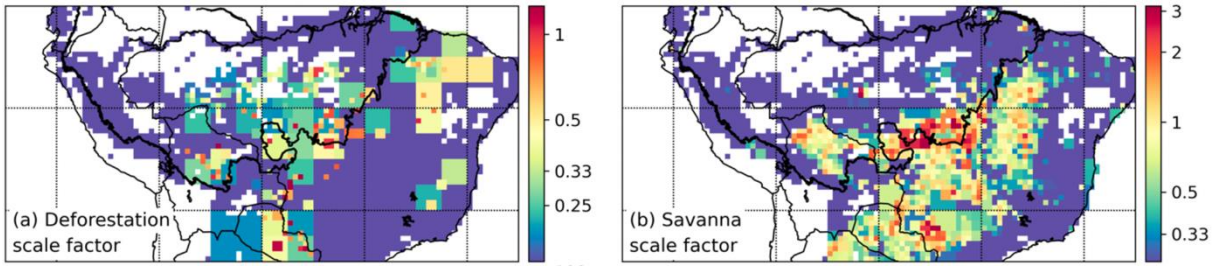

Figure 6: Burned area scaling factors used in South America. For forest fires we used a constant scaling factor of 1.0 and for small clearing and agricultural fires of 0.1.

4 TUD-S4F: Fire emissions from novel estimates of fuel loads, fuel moisture content and combustion

4.1 Theoretical baseline

Several large-scale satellite-based methods and products exist that can provide information on fuel loads, fuel moisture content (FMC), fuel consumption. Fire emissions can be then estimated from fuel consumption by applying emission factors (Andreae, 2019; van der Werf et al., 2017). Thereby, a key limitation is that current fire emission inventories use fixed average values for emission factors per biomes. Here we aim to overcome this limitation and make emission factors and hence the derived emissions dependent on the combustion efficiency and FMC for different fuel types (i.e. biomass in live leafs and wood and in litter and woody debris).

FMC can be estimated from various satellite technologies. For example, multi-spectral satellites have been frequently used to estimate the moisture content of living vegetation components (live-fuel moisture content, LFMC) (Chuvieco et al., 2002; Yebra et al., 2013). The first operational LFMC products are now available at continental and global scale (Yebra et al., 2018; Quan et al., 2021). Also observations from microwave sensors such as the Sentinel-1 radar (Wang et al., 2019; Rao et al., 2020) and vegetation optical depth (VOD) from passive microwave instruments are used to estimate LFMC (Forkel et al., 2023). Regionally is has been shown that observations from Radar satellites are also sensitive to the moisture content of surface and dead fuels (Abbott et al., 2007; Leblon et al., 2002).

Satellite-based products on fuel loads are less developed and have several limitations for the estimation of fire emissions. Only a few products have been specifically targeted to support the monitoring and modelling of fire and fire emissions. Fire-targeted products on fuel loads are for example the global fuelbed database (Pettinari and Chuvieco, 2016) and the North American Wildland Fuel Database (NAWFD) (Prichard et al., 2019). Both products combine land cover maps with representative values or statistical distributions of fuel properties such as biomass values for trees, shrubs, grass, woody debris and litter. Although both databases are specifically defined for the purpose of fire modelling and

quantifying fire emissions, their major disadvantages are that they do not provide information of the spatial variability of fuel loads within one vegetation type (fuelbed) and secondly that they do not capture any temporal changes in fuel loads.

As a first alternative, maps of canopy height and above ground biomass (AGB) from satellite retrievals could be used to quantify the spatial variability of fuel loads. Several maps of above ground biomass became available in recent years for the tropics (Saatchi et al., 2011b; Baccini et al., 2012b; Avitabile et al., 2016b), for northern ecosystems (Thurner et al., 2014), and globally (Santoro et al., 2021). The biomass dataset developed under the Climate Change Initiative (CCI) of the European Space Agency (ESA) (Biomass_cci) provides globally woody above ground biomass for the epochs 1990s, 2010s, and the years 2017, and 2018 and has a low relative error of less than 20% in areas with high biomass (Santoro et al., 2021). Because of those properties, Biomass_cci is used in Sense4Fire. Canopy height is closely related to AGB through allometric relations between tree height and biomass. Maps of canopy height are also available globally (Simard et al., 2011; Potapov et al., 2021). Although AGB and canopy height maps provide information on the regional variability of forest biomass, they have a limited use for fire-related applications because they do not provide information on different fuel components such as biomass in the canopy, wood, grass or litter and they do not provide information on the temporal dynamic of fuels.

Temporal dynamics of fuels can be approximated by satellite-derived time series of vegetation indices or biophysical parameters. Satellite-derived time series of leaf area index (LAI), the fraction of absorbed photosynthetic active radiation (FAPAR), or the fractional cover of green vegetation (fCOVER) from multi-spectral sensors, and of vegetation optical depth (VOD) from microwave sensors provide information on the temporal dynamics of vegetation cover and biomass. Several studies have demonstrated that time series of LAI, FAPAR and VOD are useful predictors for the temporal dynamics of burned area (Knorr et al., 2014; Forkel et al., 2017, 2019b; Kuhn-Régnier et al., 2021) and hence are proxies for the dynamics in vegetation fuel loads.

Here, we aim to develop an approach that combines the spatial information from remotely-sensed AGB and canopy height maps, the annual temporal information from land cover maps, and the daily to weekly temporal information from LAI and VOD time series to retrieve information on the spatial variability and temporal dynamics of fuel loads and fuel moisture content for different fuel types. Therefore, we develop an alternative approach to estimate fuel loads. The **TUD-S4F model** is a **S**atellite-based data-model fusion approach for ecosystem **F**uel load, **F**uel moisture, **F**uel consumption and **F**ire emissions and is solely driven by satellite products and can be constrained by various satellite and ground observations. Combustion completeness, fuel consumption and fire emissions are also estimated within the S4F model based on its own estimates of fuel loads. In the following, we first describe the used input datasets for and the data processing and second the structure of the S4F model.

4.2 Input data and data processing

The datasets that are currently used in the S4F model for version 2 of the ATBD and PVR are described in Table 5. Datasets are either used as input to force the S4F model, to constrain model parameters within the test areas, to calibrate parameters for certain modules of the S4F model, or to benchmark model results. The necessary input datasets to run the model are time series of LAI and soil water index and annual maps of land cover. Canopy height, AGB, LFMC and VOD are used to constrain model parameters within each study region. The Biomass and Allometry Database is used to calibrate model parameters that regulate the relationships between canopy height, leaf and woody biomass.

In order to be used as input for the S4F model, all data sets must first be harmonised to the same temporal and spatial resolution. Therefore, the extent, spatial (333 x 333 m) and temporal resolution (10-daily) of the LAI and fCOVER time series are used as reference for all other datasets because those datasets are the main inputs in the S4F model that govern most of the simulated processes.

Table 5: Overview of input and calibration datasets for the TUD-S4F and TUD-ML approaches

Variables	Dataset (Sensor)	Spatial resolution and coverage	Temporal resolution and coverage	URL
fCOVER, LAI	Sentinel-3/OLCI and Proba-V	333 m, global	10 days, Jan/2014 – Oct/2021 (281 observations)	https://land.copernicus.eu/global/products/lai
Land cover	Land cover_cci	300 m, global	annual, 1992-2020	https://www.esa-landcover-cci.org/?q=node/164
Above ground biomass (forests)	Biomass_cci	100 m, global	(1990s), 2010, 2017, 2018	http://dx.doi.org/10.5285/bedc59f37c9545c981a839eb552e4084
Forest Canopy Height	GEDI L3 Gridded Land Surface Metrics (rh100)	1 km, global (52°N-52°S)	2019-2021	https://doi.org/10.3334/ORNLDAAC/1952
Forest Canopy Height	ETH Global Canopy Top Height	10 m, global	2020	https://share.phys.ethz.ch/~pf/nlangdata/ETH_GlobalCanopyHeight_10m_2020_version1/
Ku/X/C-band Vegetation Optical Depth	VODCA VOD	0.25°, global	daily, 1987-2020 (depending on band)	https://zenodo.org/record/2575599
L-band Vegetation Optical Depth	SMOS LPRM L-VOD	0.25°, global	daily, 2010-2020	(van der Schalie et al., 2017)
Live-fuel moisture content	VOD2LFMC	0.25°, global	daily, 2000-2017	https://doi.org/10.5281/zenodo.6545571
Soil water index	Metop-ASCAT	0.1°, global	10 days, since 2007	https://land.copernicus.eu/global/products/swi
Burned area	Fire_cci 5.1, MODIS	250 m, global	Monthly with first day of detection	https://dx.doi.org/10.5285/58f00d8814064b79a0c49662ad3af537

Fuelbed classification fuel loads	NAWFD (Prichard et al., 2019)	26,620 in-situ observations, ~ 30 m (EVT map)	--	https://fuels.mtri.org
Tree allometry, biomass in tree components	BAAD (Falster et al., 2015)	Measurements from single trees from laboratories and field sites	--	https://doi.org/10.6084/m9.figshare.c.3307692.v1
Fuel loads and consumption	Updated fuel consumption database	Measurements from field sites	--	(original by van Leeuwen et al., 2014; updated by van Wees et al., 2022)
Live-fuel moisture content	Globe-LFMC	Measurements from field sites	--	(Yebra et al., 2019)
Litter pools	Global Database of Litterfall Mass and Litter Pool Carbon	Measurements from field sites	--	(Holland et al., 2014),
Emission factors, combustion efficiency	Emission factor database	Measurements from field sites and laboratories	--	Andreae (2019)

4.2.1 LAI and fCOVER

LAI and fCOVER from Sentinel-3 OLCI and Proba-V, Version 1.1 (Fuster et al., 2020) are used. Leaf area index (LAI) and the fraction of green vegetation cover (fCOVER) are available at a resolution of 333 m. The product has been available since January 2014 as near-real time 10-daily product. Version 1.0 of the algorithm uses Proba-V observations as input, version 1.1 uses Sentinel-3/OLCI observations. The estimation of the biophysical parameters is performed using neural networks. The production of LAI and fCOVER estimates includes a temporal smoothing and gap filling to reduce noise in time series. Observations from several days are combined in a 10-daily near-real time estimate. This estimate is then changed to a consolidated value after two months of observations (Verger and Descals, 2021). The combined Sentinel-3/OLCI and Proba-V LAI and fCOVER product are available from the Copernicus Global Land Service: https://land.copernicus.eu/global/products/lai.

For each study region subsets have been created. The LAI as well as the fCOVER time series range from January 2014 to October 2021 (281 observations, 36 observations per full year). Permanent gaps in LAI/FCOVER time series that occur regularly during winter months were filled with the observed minimum values. Any other gaps were filled by linear interpolation.

4.2.2 Land cover / tree cover

Land cover maps provide information about the type of vegetation and hence the susceptibility of land to fire occurrence (Vilar et al., 2019). Land cover maps were taken from the ESA CCI data set. The ESA CCI provide annual maps of the distribution of land cover classes for the years 1992 to 2020 at 300 m spatial resolution. The annual maps were introduced by the dataset creators and by ESA with the purpose to investigate land cover changes and after applying a cross walking approach, estimates of land cover

changes are comparable with other datasets at large scales (Li et al., 2018). In the production of the CCI land cover dataset a multi-year filtering was applied to reduce unrealistic changes, which however likely results in an underestimation of real land cover changes. Time series of vegetation indices or biophysical variables show stronger inter-annual to decadal dynamics. Here, we additionally use the trend component of LAI as a predictor for tree height, which allows passing the long-term changes in LAI to our estimates of forest height, and hence biomass pools.

We aggregate the land cover information from ESA CCI to the fractional coverage of different plant functional types (PFT) by using the cross-walking approach (Poulter et al., 2015). In a second step, we aggregate the fractional coverage of different PFTs to two main classes: fraction of tree cover and fraction of herbaceous cover.

For simplicity, we include the area fraction of shrub PFTs (f_{shrub}) into the fraction of tree cover (f_{tree}) and combine grass cover (f_{grass}) with the fraction of crop cover (f_{crop}):

$$f_{tree} = \sum_{p=1}^{n} f_{tree,p} + \sum_{p=1}^{n} f_{shrub,p} \quad (4.1)$$

$$f_{herb} = f_{grass} + f_{crop} \quad (4.2)$$

To ensure consistency with the canopy height dataset, we examined the distribution of canopy heights within the PFT classes. This analysis showed that shrub-dominated areas also have canopy heights > 1 m.

To further test how a land cover dataset with stronger temporal dynamics affects the results, we additionally used in one experiment for the Amazon study region the dataset by Song et al. (2018). The dataset provides annual maps of fractional cover of trees and short vegetation for the period 1982-2016, which we used between 2014 and 2016 and by repeating the map from 2016 until 2021.

The annual maps of coverage fractions are repeated 36 times per year to match the time steps of the LAI and fCOVER data. This can lead to abrupt jumps between successive years. These could be avoided by interpolation, but is not feasible without the addition of further data sources and making assumptions about the development of vegetation fractions. Finally, we perform a spatial resampling to match with the raster grid of the LAI data set.

4.2.3 Above ground biomass

The above ground biomass (AGB) from Biomass_cci is available at 100 m spatial resolution for the years 1990s, 2010, 2017 and 2018 (Santoro et al., 2021). The dataset provides the total AGB of all woody components (stem, bark, branches, and twigs) of trees and comes with an estimate of uncertainty. We use the AGB from 2017 and 2018 as input to our methodology to estimate fuel loads by providing an upper constraint on the total woody AGB within a grid cell. Therefore the AGB datasets is kept as a static map, only a spatial resampling to the LAI dataset was performed (Santoro et al., 2021). Therefore the dataset is resampled to the same spatial resolution as the LAI data calculating the mean value and then matched to the LAI pixel grid using nearest neighbour interpolation. Finally

the units were converted from Mg/ha to kg/m^2. For the use in in the calibration of the S4F model the values between 2010, 2017 and 2018 were linearly interpolated to daily values for the comparison with the 10-daily outputs of the S4F model.

4.2.4 Canopy height

We used the GEDI L3 product for the calibration and validation of the tree height computation (Section 4.3.2). The GEDI L3 Gridded Land Surface Metrics product provides gridded mean canopy height, based on the first reflection off the top of canopy (rh100) at 1 km spatial resolution.

As GEDI does not cover latitudes > 52°N, the ETH Global Canopy Top height dataset was used for the Siberia test area. The ETH dataset combines estimates of canopy height from the GEDI space-borne Lidar with observations from Sentinel 2 to produce a global map of forest canopy height at 10 m spatial resolution. Hence north of 52°N, the estimates of canopy height are solely based on the Sentinel-2 data. After a comparison of these canopy height product (see PVR v2, Section 3.2.1), the ETH dataset has some artefacts (sharp edges with changing canopy heights), which seems to originate from the used Landsat tiles.

To correspond with the LAI data, all datasets are resampled to the same spatial resolution as the LAI data calculating the mean value and then matched to the LAI pixel grid using nearest neighbour interpolation.

4.2.5 Vegetation Optical Depth

Vegetation Optical Depth (VOD) in short (Ku-band, ≈ 1.6-2.5 cm; X-band, ≈ 3 cm; C-band, ≈ 5.6 cm) and longer wavelengths (L-band, 23 cm) is sensitive to the water content of leaves/twigs and branches/stems, respectively. Short-wavelength VOD was taken from the VODCA dataset (Moesinger et al., 2020) and L-band from the SMOS-LPRM retrieval (van der Schalie et al., 2017). VODCA provides harmonised time series of VOD in Ku-, X- and C-bands at 0.25° spatial resolution and daily temporal resolution for the period 1987-2017, 1997-2018, and 2002-2018, respectively (Moesinger et al., 2020).

The SMOS-LPRM retrieval dataset provides time series of VOD in L-band at 0.25° spatial resolution and daily temporal resolution for the period 2010-2020 (van der Schalie et al., 2017).The VOD datasets are used to constrain parameters of the S4F model with respect to the temporal dynamics in fuel moisture and biomass at large scales. Thereby we assume that Ku- and X-VOD are mostly sensitive to the vegetation water content (VWC) in the canopy while L-VOD has a higher sensitivity to woody VWC. C-VOD was not further used because of the high similarity with Ku- and X-VOD and because it shows stronger effects of RFI after 2017.

We apply the same pre-processing steps to all VOD band. This comprises a temporal sub-setting to the interval that matches the LAI time series, a spatial resampling to the LAI grid

using nearest neighbour interpolation and finally a temporal resampling to the LAI time series. For the temporal resampling we calculate the mean for each 10-days-interval.

4.2.6 Soil water index

The soil water index from Metop/ASCAT is a proxy for soil moisture in various depths. The dataset is available at a resolution of 0.1° for the period since 2007 (Bauer-Marschallinger et al., 2018). The SWI is used as proxy for surface fuel moisture. The SWI might be not fully reliable as proxy for soil moisture over dense tropical forests because of the attenuation of microwaves in the vegetation layer. However, we assume that soil and vegetation moisture are correlated which allows using the SWI. The SWI dataset is already available as a 10 day product, which uses the same 10 day interval as the LAI dataset. Therefore, temporal resampling is not necessary. We use a temporal subset of the SWI time series from January 2014 to October 2021 (observation period of the LAI time series), which is resampled to the spatial resolution of the LAI data set using nearest neighbour interpolation.

4.2.7 Live-fuel moisture content

The VOD2LFMC live-fuel moisture content (LFMC) dataset (Forkel et al., 2023) provides daily estimates of LFMC at a spatial resolution of 0.25° for the period February 2000 to July 2017. The LFMC estimates were used to calibrate the computations of LFMC from the S4F model. We apply the same pre-processing steps as for the VOD bands. This comprises a temporal sub-setting to the interval that matches the LAI time series, a spatial resampling to the LAI grid using nearest neighbour interpolation and finally a temporal resampling to the LAI time series. For the temporal resampling we calculate the mean for each 10-day interval.

4.2.8 Burned area and fire radiative energy

Several burned area products were tested in the test areas as input to the S4F model. Specifically, we used the burned area data as described in section 3.5 and the ESA CCI burned area product version 5.1 (Lizundia-Loiola et al., 2020). As the ESA CCI burned area product is readily available for all study regions, we used this product as the main input in the S4F model in all study regions and for the results described in PVRv2.1.

Fire radiative energy (FRE) was taken from Sentinel-3 SLSTR and VIIRS observations as described in section 3.3 to calibrate the S4F model.

4.2.9 Databases of ground observations

We use several databases of ground observation to constrain parameters of the S4F model to validate the SF4 model.

The Biomass and Allometry Database (BAAD) provides information on biomass stocks in different tree components such as stems, branches, leaves and roots (Falster et al., 2015). The database includes 259,634 measurements from 176 studies and 678 tree species. The

measurements cover all major biomes and a wide range in biomass. The spatial representativeness of the database cannot be fully assessed because some measurements originate from greenhouses and gardens. We use BAAD to constrain parameters of the allometry module of the S4F model that represent the relationships between tree height, stems, branches and leaf biomass.

For validation of further model components, the global live-fuel moisture content database (Globe-LFMC) (Yebra et al., 2019), the Global Database of Litterfall Mass and Litter Pool Carbon (Holland et al., 2014), the updated field measurement database of fuel loads and biomass burning fuel consumption (van Wees et al., 2022) and the compilation of emission factory by Andreae (2019) were used.

4.3 TUD-S4F: S4F data-model fusion approach

4.3.1 Overview of the model structure

The S4F model takes satellite-based time series of the fractional coverage of trees and herbaceous vegetation, LAI, SWI, and burned area as input and provides estimates of the temporal dynamics of fuel loads (FL) and fuel moisture, combustion completeness (CC), fuel consumption and fire emissions (Figure 7). Thereby the S4F model follows the classical bottom-up approach as for example used in GFED (Andreae and Merlet, 2001; van der Werf et al., 2006, 2010, 2017) to estimate fire emissions (E) from fuel consumption (FC) and emission species-specific emission factors (EF_x):

$$E_x = BA \times FC \times EF_x = BA \times CC \times FL \times EF_x \quad (4.3)$$

Unlike in other fire emission inventories, we do not use fixed biome-dependent emission factors but estimate emission factors dynamically dependent on the fuel types and fuel moisture by using a simple chemical-based combustion model (chapter 4.3.10). The combustion model is calibrated against the emission factor database from Andreae (2019).

The model represents different fuel types such as tree leaves, branches and stems, herbaceous vegetation, surface litter and fine and coarse woody debris (FWD, CWD). For FL, allometric equations are used to estimate the biomass in tree stems, branches and leaves from canopy height and LAI is used to estimate temporal changes in herbaceous biomass, carbon turnover and the production of litter, FWD and CWD. CC is estimated from fuel moisture, which is estimated for tree leaves and herbaceous vegetation (i.e. live-fuel moisture content) and for wood, and SWI is used as proxy for the moisture content of surface fuels.

The model also simulates vegetation optical depth (VOD) and fire radiative energy (FRE). Hence, satellite datasets of VOD, FRE, LFMC, canopy height and total woody biomass can be used for comparisons with the model estimates and to calibrate model parameters. As the model structure provides the ecological and biophysical relations between various ecosystem properties, it allows linking various satellite products in one consistent

framework. By inverting the S4F model against satellite products of canopy height, AGB, LFMC, VOD and FRE, the load and moisture content and consumption of different fuel types can be estimated and hence provide a bottom-up constrain on fuel consumption and fire emissions.

The S4F model computes the different components in the following order:

1. The temporal dynamics in tree height is computed from long-term changes in mean LAI and the fractional tree cover. The estimated tree height is calibrated against the canopy height dataset. Canopy height is not used as direct input to the model because it does not provide any information on temporal changes in tree height.
2. The estimated tree height is used in the allometry module to estimate stem biomass and consecutively branches and leaf biomass. Thereby temporal changes of tree height as estimated in Step 1 directly translate into changes in stem, branches and leaf biomass.
3. The temporal dynamic of herbaceous biomass is directly estimated from the temporal changes in LAI.
4. Biomass turnover from living vegetation to the surface (e.g. leaf fall, transfer of woody biomass) is estimated from the temporal changes in leaf and woody biomass, which originate from the temporal changes in LAI and tree cover.
5. Surface litter and fine and coarse woody debris (FWD and CWD) are estimated from the biomass turnover from leaves, branches and stems, respectively. The decomposition of litter, FWD and CWD is represented through simple decomposition rates.
6. LFMC is estimated from LAI and SWI and calibrated against LFMC datasets. The moisture content of wood is approximated as linear regression with leaf LFMC and SWI. L-VOD data is then used to parametrise this relationship.
7. Satellite SWI is used as proxy for the fuel moisture content of surface fuels (litter, FWD and CWD).
8. The estimates of leaf and woody fuel moisture content and of above ground biomass are then used to compute vegetation water content (VWC) and to estimate VOD for different wavelengths.
9. Combustion completeness is implemented as a linear function of FMC for leaves and wood, and as linear function of SWI for litter, FWD and CWD.
10. Fuel consumption is then simulated based on eq. 4.3 separately for leaves, wood, herbaceous vegetation, litter, FWD and CWD.
11. The consumed fuel load is then used in the chemical-based fire combustion model (Rego et al., 2021) to estimate heat yields (fire radiative energy) and emission factors. The model approach allows estimating emission factors dependent on fuel moisture content and fuel composition and hence might provide a major advancement over approaches that use fixed emission factors per biome.
12. The emission factors are multiplied with the fuel consumption to receive total emissions.

In the following, we describe the implementation of the different modules of version 0.2 of the S4F model and describe the calibration setup. Results of the S4F model for each calibration step and validations with independent data are presented in the PVRv2.

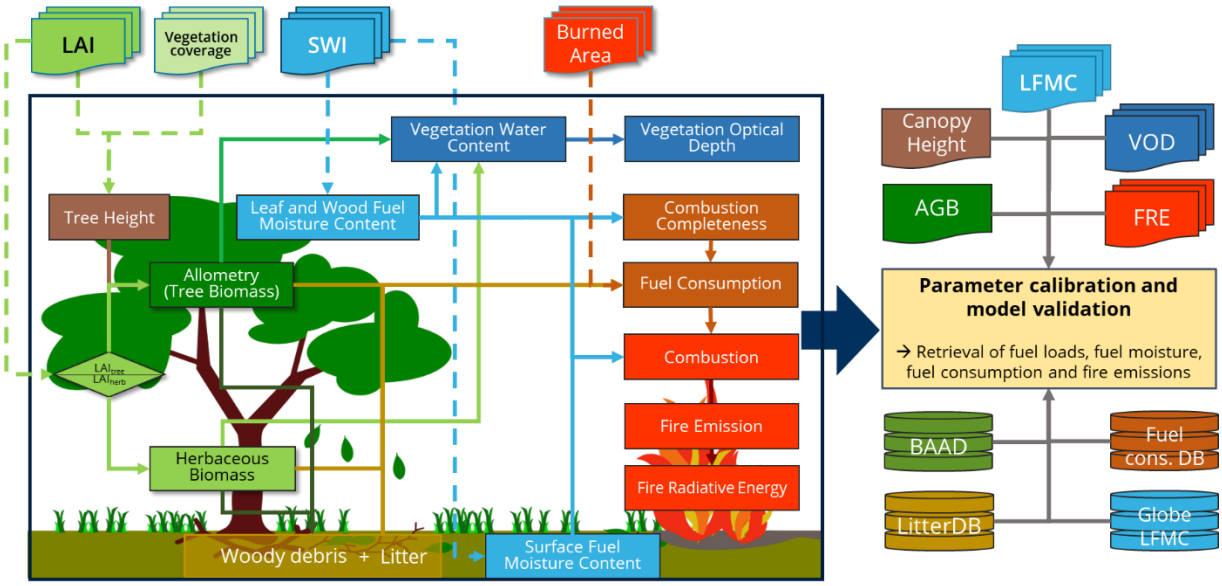

Figure 7: Simplified structure of the S4F model with forcing data (top) and data used for local calibration and model validation (right).

4.3.2 Tree canopy height

To compute temporal changes in canopy height, we follow a space-for-time approach and assume that the spatial patterns of mean LAI and fractional tree cover are plausible predictors for the temporal changes in tree height.

Long-term changes in mean LAI (LAI_{mean}) are based on the trend component of the LAI time series. Therefore, we used the Seasonal Decomposition of Time Series by Loess (STL) method (Cleveland et al., 1990) to decompose the LAI time series into a periodic seasonality, a trend component and the short-term remainder:

$$LAI_{mean} = STL(LAI_{obs}) \quad (4.4)$$

Tree height *H* can then be computed from LAI_{mean} and the fractional tree cover f_{tree} based on any regression model function *f()*:

$$H = h1 \times f(LAI_{mean}, f_{tree}) + h2 \quad (4.5)$$

We tested several regression models for f(), such as linear regressions, second-order polynomial regression, quadratic regression, generalised additive models and random forest. The results of this analysis are presented in PVRv2. The parameters *h1 and h2* are used as scalars to fit the estimated tree height from the regression model to the canopy height data of individual grid cells, i.e. to eliminate any local biases from the regression model. All parameters with the chosen prior values are listed in Table 6.

Table 6: Overview of parameters and prior values for the S4F model.

Name (unit)	Prior value	Lower	Upper	Description and use	Reference
h1	1	0.7	1.3	Scalars for canopy height	Calibration against canopy height
h2	0.001	-10	10		
a1 (kg m-2)	0.0199	0.001	0.7	Allometric relation between tree height and stem biomass	Estimation of parameters based on calibration against BAAD
a2	0.4666	0.1	1.5		
a3	0.2095	0.05	2.5	Allometric relation between stem biomass and branches biomass	
a4	0.9244	0.3	2		
a5	0.1172	0.1	2.5	Allometric relation between stem biomass and leaves biomass	
a6	2.3018	0.5	3.5		
sla (m^2/kg)	25	8	70	Specific leaf area to compute herbaceous biomass from LAI	(Reich et al., 1998)
t_leaf (yr^{-1})	0.5	0.2	1	Constant baseline turnover rate for leaves	(Kikuzawa et al., 2013)
t_wood (yr^{-1})	0.0319	0.01	0.5	Constant baseline turnover rate for stem and branches	(Johnson et al., 2016)
fsb	0.2	0.05	0.95	Fraction of small branches (diameter < (3" = 7.62 cm) for turnover of branches biomass to FWD or CWD	Not yet calibrated
k_l (yr^{-1})	0.94	0.047	4.66	Litter decomposition rate	Value for tropical forests (Harmon et al., 2020)
k_fwd (yr^{-1})	0.564	0.0282	2.796	FWD decomposition rate	Value for tropical forests (Harmon et al., 2020)
k_cwd (yr-1)	0.188	0.0094	0.932	CWD decomposition rate	Value for tropical forests (Harmon et al., 2020)
f0_leaf	0.8	0.005	1.699	Inflection point of relationship to LFMC, value for broadleaved trees	Estimation of parameters based on calibration against Globe-LFMC
f0_herb	0.964	0.005	1.939	Inflection point of relationship to LFMC, value for herbaceous vegetation	
f1_leaf	1.012	-0.457	2.461	Weighting of LAI in the computation of LFMC, value for broadleaved trees	
f1_herb	1.403	0	3.577	Weighting of LAI in the computation of LFMC, value for herbaceous vegetation	
f2_leaf	1	-371.4	211.871	Weighting of SWI in the computation of LFMC, value for broadleaved trees	
f2_herb	1	-250.774	291.860	Weighting of SWI in the computation of LFMC, value for herbaceous vegetation	
m1 (%)	20	10	100	Minimum moisture content of living wood	(Glass and Zelinka, 2010)

m2 (%)	150	40	300	Maximum moisture content of living wood	
b0	0.61	0.2	2	Relationship between wavelength and VOD	(Jackson and Schmugge, 1991)
b1	-0.528	-2	-0.2		
w1 (cm)	70	20	500	Wavelength at which only wood contributes to VOD	Calibration against multi-frequency VOD time series
c1_leaf (%)	250	30	300	Maximum FMC of leaves at which combustion completeness = 0	Prior c2 parameters like in van der Werf et al. (2006, 2010); and additional calibration against fire radiative energy
c2_leaf	0.95	0.9	1	Maximum combustion completeness of leaves	
c1_wood (%)	150	30	200	Maximum FMC of wood at which combustion completeness = 0	
c2_wood	0.3	0.2	0.4	Maximum combustion completeness of living wood	
c1_litter (%)	100	30	200	Maximum SWI of litter at which combustion completeness = 0	
c2_litter	0.9	0.8	1	Maximum combustion completeness of litter	
c1_fwd (%)	100	30	200	Maximum SWI of FWD at which combustion completeness = 0	
c2_fwd	0.7	0.5	0.9	Maximum combustion completeness of FWD	
c1_cwd (%)	100	30	200	Maximum SWI of CWD at which combustion completeness = 0	
c2_cwd	0.5	0.3	0.7	Maximum combustion completeness of CWD	
fvo_leaf	0.1	0	0.5	Fraction of volatiles in leaves	
fce_leaf	0.46	0.4	0.7	Fraction of cellulose in leaves	Rego et al. 2021
fvo_herb	0.1	0	0.5	Fraction of volatiles in herbs	
fce_herb	0.35	0.3	0.45	Fraction of cellulose in herbs	Rego et al. 2021, Waliszewska et al. 2021
fce_wood	0.7	0.4	0.9	Fraction of cellulose in wood	Rego et al. 2021
eofr_leaf	0.95	0.8	0.96	Equivalent oxygen to fuel ratio for combustion of leaves	Rego et al. 2021
eofr_herb	0.95	0.8	0.96	Equivalent oxygen to fuel ratio for combustion of herbaceous	Rego et al. 2021
eofr_wood	0.88	0.8	0.96	Equivalent oxygen to fuel ratio for combustion of wood	Rego et al. 2021
eofr_litter	0.96	0.8	0.96	Equivalent oxygen to fuel ratio for combustion of litter	Rego et al. 2021
eofr_fwd	0.88	0.8	0.96	Equivalent oxygen to fuel ratio for combustion of FWD	Rego et al. 2021
eofr_cwd	0.88	0.8	0.96	Equivalent oxygen to fuel ratio for combustion of CWD	Rego et al. 2021
nox_a	6.678	1.2	12.1	Emission factor for NOx: EF_NOx = nox_a * MCE + nox_b	Estimated from Andreae et al. 2019

nox_b	-3.712	-8.62	1.41	Emission factor for NOx: EF_NOx = nox_a * MCE + nox_b	Estimated from Andreae et al. 2019

4.3.3 Tree biomass

After the computation of tree height, allometric equations are used to compute the biomass in stems, branches and leaves. Stem biomass BM_{stem} is computed from tree height based on an exponential function:

$$BM_{stem} = a1 \times H^{\frac{1}{a2}} \quad (4.6)$$

Whereby a1 and a2 are the parameters of this relationship. Following the definition of the allometric equations that were used for the map of above ground biomass for temperate and boreal forests (Thurner et al., 2014), we then use BM_{stem} to compute the biomass of tree branches $BM_{branches}$ and leaves BM_{leaves} as:

$$BM_{branches} = a3 \times BM_{stem}^{\frac{1}{a4}} \quad (4.7)$$

$$BM_{leaf} = a5 \times BM_{stem}^{\frac{1}{a6}} \times P \quad (4.8)$$

Whereby a3 to a6 are the parameters (Table 6) and P is phenology status of tree canopies. P is zero in case of no leaf cover and one in case of full leaf cover. The phenology status is directly computed from the CGLS fCOVER dataset:

$$P = \frac{fCOVER - fCOVER_{min}}{fCOVER_{max} - fCOVER_{min}} \quad (4.9)$$

Whereby $fCOVER_{min}$ and $fCOVER_{max}$ are the minimum and maximum fCOVER values of a grid cell, respectively. Above ground woody biomass BM_{wood} and total tree biomass BM_{total} are then computed as:

$$BM_{wood} = a0 \times (BM_{stem} + BM_{branches}) \quad (4.10)$$

$$BM_{total} = BM_{wood} + BM_{leaf} \quad (4.11)$$

Whereby the parameter a0 is used as scaling factor to fit the estimated woody biomass of each grid cell against the woody biomass of the ESA CCI biomass map (2018). If a0 is different from 1, BM_{stem} and $BM_{branches}$ are re-scaled in order to fit the scaled BM_{wood}.

4.3.4 Herbaceous biomass

Herbaceous biomass is directly estimated from LAI because several studies report linear relationships between LAI and grass biomass (Punalekar et al., 2018; Schwieder et al., 2020; Makuma-Massa et al., 2017). Thereby, we make use of the relation between herbaceous biomass BM_{herb}, herbaceous LAI LAI_{herb} and the specific leaf area sla:

$$BM_{herb} = \frac{LAI_{herb}}{sla} \quad (4.12)$$

The herbaceous LAI within a pixel is estimated from the observed LAI and the fractional coverages of trees f_{tree} and herbaceous vegetation f_{herb}:

$$LAI_{herb} = \frac{f_{herb}}{f_{tree}+f_{herb}} \times LAI_{obs} \quad (4.13)$$

The LAI of trees LAI_{tree} is accordingly estimated as the difference between LAI and LAI_{herb}. This splitting approach of LAI into the contribution of tree and herbaceous vegetation assumes that both types have the same phenology and that LAI scales directly with vegetation cover, which might be an over-simplification.

4.3.5 Biomass turnover and surface fuel dynamics without fire

The turnover *T* of vegetation biomass to surface fuels is estimated from a constant baseline turnover (eq. 4.14) and from the temporal differences in the estimated biomass of leaves, branches, stem, and herbaceous vegetation (eq. 4.15):

$$T_{B,i} = BM_i \times (1 - e^{-t_i}) \quad (4.14)$$

Whereby the parameter t_i is a constant turnover rate, which is defined for leaves and wood separately.

$$T_i = \begin{cases} \Delta BM_i = T_{B,i} + (BM_{i,t-1} - BM_{i,t}), & \Delta BM_i > 0 \\ T_{B,i}\,, & \Delta BM_i < 0 \end{cases} \; with\; i \in \{leaf, herb, branches, stem\}, t = time \quad (4.15)$$

For example, the biomass transferred from canopy leaves or herbaceous vegetation to surface litter during leaf fall is computed as the difference between leaf biomass between two consecutive time steps and ultimately depends on the temporal dynamic of fCOVER (eq. 4.9) and LAI (eq. 4.12), respectively. The turnover of branches and stem biomass to FWD and CWD is calculated accordingly and hence depends on the estimated temporal changes in tree height (eq. 4.5, 4.6), which itself depends on the long-term change in mean LAI and the observed changes in tree cover (eq. 4.4 and 4.5).

Based on these turnover fluxes of carbon, we estimate the dynamics of litter (L), FWD and CWD. Following the definitions in the NAWFD (Prichard et al., 2019), L is dead leaf or herbaceous material, and FWD and CWD are dead woody material with a diameter threshold below and above 3" = 7.62 cm, respectively. Please note that we currently do not distinguish between standing and lying CWD.

To estimate initial values of L, FWD and CWD fuel loads, we assume that those carbon pools are in steady state, i.e. the input of carbon from turnover equals the release of carbon through decomposition (heterotrophic respiration). The steady state assumption was previously applied to remotely sensed estimates of gross primary production, above ground biomass and of soil carbon stocks to estimate total ecosystem carbon turnover times globally (Carvalhais et al., 2014; Fan et al., 2020). Following these studies, the carbon turnover time τ of a system is related to the carbon stock *S* and the carbon flux *F* (either gross primary production or ecosystem respiration) as:

$$\tau = \frac{S}{F}\ [yr] \quad (4.15)$$

The annual turnover rate *k* (yr^{-1}) is related to the annual turnover time (yr) as $k = 1/\tau$. Following these equations and assuming steady state, we estimate the initial carbon stock

(or fuel load) as the ratio of the carbon flux (i.e. turnover from falling leaves and wood to the surface) and the turnover rate ($S = F / k$). Hence, the initial load of litter $L_{t=0}$ is computed from total turnover from leaf fall and herbaceous biomass over all time steps *t*:

$$L_{t=0} = \frac{\sum_{t=1}^{n} T_{leaf} + T_{herb}}{nyears \times k_{litter}} \quad (4.16)$$

Whereby *nyears* is the number of years over which the summation is applied and k_{litter} is the annual litter decomposition rate. The initial loads of FWD and CWD are computed accordingly from the turnover of branches and stems:

$$FWD_{t=0} = \frac{(\sum_{t=1}^{n} T_{branches}) \times f_{sb}}{nyears \times k_{fwd}} \quad (4.17)$$

$$CWD_{t=0} = \frac{\sum_{t=1}^{n} (T_{stem} + T_{branches} \times (1 - f_{sb}))}{nyears \times k_{fwd}} \quad (4.18)$$

Whereby f_{sb} is the fraction of small branches with diameter < 7.62 cm, which regulates how much branch biomass is transferred to FWD or CWD, respectively. Please note that the amount of CWD in an ecosystem depends especially on the time since the last disturbance, the disturbance type and the stand age (Sturtevant et al., 1997; Pedlar et al., 2002; Harmon et al., 2020). As such information is not directly available from Earth observation data over large areas, we intend to approximate the involved dynamics by using multi-annual time series of LAI and of f_{tree} to potentially capture past disturbance events.

Starting from the initial estimates, we then compute the temporal dynamics of L, FWD and CWD from the turnover *T* and the daily decomposition *D*:

$$L_t = L_{t-1} + T_{leaf,t} + T_{herb,t} - D_{litter,t} \quad (4.19)$$

$$FWD_t = FWD_{t-1} + T_{branches,t} \times f_{sb} - D_{fwd,t} \quad (4.20)$$

$$CWD_t = CWD_{t-1} + T_{branches,t} \times (1 - f_{sb}) + T_{stem,t} - D_{cwd,t} \quad (4.21)$$

Whereby the daily decomposition for the three fuel types simply depends on the annual decomposition rate k:

$$D_{i,t} = S_{i,t} \times \left(1 - e^{-\frac{k_i}{tsy}}\right), with\ S_i \in \{L, FWD, CWD\} \quad (4.22)$$

The parameter *tsy* defines the number of time steps per year (e.g. tsy = 36 in case of 10 daily time steps) and distributes the annual decomposition rate k_i to an estimate for each time step. Note that this is a strong simplification as the daily decomposition rate depends strongly on daily variations in temperature and soil moisture.

4.3.6 Fuel moisture and vegetation water content

Fuel moisture content in forest fire research is commonly defined as the amount of water over the dry biomass of a vegetation sample (Yebra et al., 2013) and hence is related to wet biomass (BM_{wet}) and dry biomass (BM_{dry}) and vegetation water content (*VWC*) as:

$$FMC = \frac{BM_{wet} - BM_{dry}}{BM_{dry}} \times 100\% = \frac{VWC}{BM_{dry}} * 100\% \quad (4.23)$$

FMC is commonly distinguished for living and dead vegetation components (LFMC and DFMC). In the S4F model, FMC is represented by live fuels (e.g. LFMC of leaves and herbaceous vegetation) and for wood. The moisture content of dead fuels (L, FWD and CWD) is not specifically represented but we use the soil water index (SWI) of the upper layer as proxy for dead fuel moisture content. Please note that the range of FMC is usually between 0 and 400% (Yebra et al., 2019) whereas SWI represents the percentage of soil saturation (0-100%).

LFMC can be obtained from external datasets and can be prescribed into the S4F model or alternatively can be estimated from LAI and SWI because LFMC, LAI and SWI are highly correlated in many ecosystems. We estimate FMC of leaves and herbaceous vegetation based on a single-layer perceptron (as used in neural networks) with a sigmoidal activation function by using LAI and SWI as input:

$$FMC_i = \frac{400\%}{1+e^{-(z-f_0)}} \quad (4.24)$$

$$z = \left(f1 \times \frac{LAI - LAI_{min}}{LAI_{max} - LAI_{min}}\right) + \left(f2 \times \frac{SWI - SWI_{min}}{SWI_{max} - SWI_{min}}\right) \quad (4.25)$$

Whereby the sigmoidal activation function ensures that LFMC is scaled to plausible ranges between 0% and 400%. Equation 4.25 is a weighted sum, which takes normalised LAI and SWI values. The normalisation is based on the temporal minimum and maximum LAI and SWI in each grid cell. The parameters *f0*, *f1* and *f2* were calibrated for different vegetation types based on LFMC observations from the Globe-LFMC database (see PVRv2).

Woody FMC (FMC_{wood}) is assumed to increase linear with leaf FMC. FMC_{wood} equals to a minimum woody moisture content *m1* if $FMC_{leaf} \leq 10\%$ and increases up to a maximum woody moisture content *m2* at the 99%-ile of FMC_{leaf}.

The vegetation water content (VWC) for leaves, wood and herbaceous vegetation is then computed as:

$$VWC_i = BM_i \times FMC_i \quad (4.26)$$

4.3.7 Vegetation optical depth

Vegetation optical depth (VOD) describes the attenuation of microwave radiation in the vegetation layer and is related to VWC, FMC and dry biomass as (Jackson and Schmugge, 1991; Konings et al., 2019):

$$VOD_\lambda = b_\lambda \times VWC = b_\lambda \times BM_{dry} \times FMC \quad (4.27)$$

Whereby the parameter *b* defines the relationship between VOD and the wavelength λ of the microwave radiation. While longer wavelengths can more penetrate the vegetation layer and hence are more sensitive to woody components of vegetation, shorter wavelengths have a weaker penetration depth and are more sensitive to tree canopies (Saatchi and Moghaddam, 2000). According to Jackson and Schmugge (1991), the

parameter b in the VOD-VWC relationship can be expressed based on a logarithmic relationship with wavelength:

$$b_\lambda = b0 \times \lambda^{b1} \quad (4.28)$$

Whereby the parameters *b0* and *b1* define the shape of the relationship. We estimate the parameters with *b0* = 0.61 and *b1* = -0.528 based on the measurements reported in Jackson and Schmugge (1991).

In the S4F model, leaves, wood and herbaceous vegetation contribute to the overall estimate of vegetation water content. In order to account for those different components on VOD, we define here VOD as a function of woody, herbaceous and leaf VWC:

$$VOD_\lambda = b_\lambda \times (VWC_{wood} \times f_{wood,\lambda} + (VWC_{herb} + VWC_{leaf}) \times (1 - f_{wood,\lambda})) \quad (4.29)$$

Whereby the parameter f_{wood} describes the fractional contribution of wood to the overall VWC for which a certain wavelength is sensitive. Hence we assume that f_{wood} depends on wavelength and is zero outside the microwave domain (f_{wood} = 0 for λ < 0.1 cm) and linearly increases to 1 at a certain wavelength *w1*. We assume that the value of *w1* is larger than 20 cm (e.g. L-band at $\lambda \approx$ 23 cm) and hence only long wavelengths have a complete contribution of woody VWC to VOD. The parameter *w1* was calibrated for each grid cell based on satellite VOD data. According to equation 4.29, the attenuation of microwaves will be stronger at vegetation with high water content and biomass (trees) than at herbaceous vegetation and will be stronger for shorter than for longer wavelengths.

4.3.8 Combustion completeness and fractional burning

Following the approach which is used in GFED (van der Werf et al., 2006, 2010, 2017), we likewise estimate combustion completeness CC as a function of fuel moisture content. In GFED CC depends on modelled soil moisture. In the S4F model, the CC of leaves and wood depends on leaf and woody FMC, respectively, and the CC of litter, FWD and CWD depends on SWI. CC declines linearly with FMC with CC = 0 at a maximum FMC or SWI for combustion (parameter c1) and a maximum combustion completeness (parameter *c2*) at FMC or SWI = 0):

$$CC_i = \begin{cases} 0 \ \ if \ FMC_i > c1_i \\ c2_i \ \ if \ FMC_i = 0 \end{cases} \quad (4.30)$$

Parameters c1 and c2 are calibrated to fit observed regional statistical distributions of CC from the updated fuel consumption database by (van Wees et al., 2022) .

The fractional burned fuel load f_{burn} is then computed for each fuel type as the product of CC and the fractional burned area per grid cell:

$$f_{burn,i} = fBA \times CC_i \quad (4.31)$$

4.3.9 Fuel consumption dynamics

Fuel consumption is then computed for each fuel type separately. Fuel consumption for living vegetation components (leaves, branches, stem and herbaceous vegetation) is only

computed when the used input datasets of LAI and tree cover suggest a reduction in LAI and/or tree cover. If we do not find a reduction in the two satellite datasets, we assume that the fire did not affect the living vegetation components but only litter, FWD and CWD. To achieve this, we compute fuel consumption for living vegetation components not based on the estimated fuel loads but based on the estimated turnover between two time steps (eq. 4.14):

$$FC_{i,t} = T_{i,t} \times f_{burn,i,t}, with\ i \in \{leaf, herb, branches, stem\} \quad (4.32)$$

The fuel consumption of litter, FWD and CWD depends on the available fuel loads at a time step:

$$FC_{i,t} = S_{i,t} \times f_{burn,i}, with\ S_i \in \{L, FWD, CWD\} \quad (4.33)$$

Total fuel consumption is the sum across the different fuel types:

$$FC_{total} = FC_{leaf} + FC_{branches} + FC_{stem} + FC_{herb} + FC_L + FC_{FWD} + FC_{CWD} \quad (4.34)$$

Following the computation of L, FWD and CWD in equations 6.18-6.21, the surface fuel loads are in the case of fire computed as:

$$L_t = (L_{t-1} + [T_{leaf,t} - FC_{leaf,t}]) \times d_{litter} \times (1 - f_{burn,litter,t}) \quad (4.35)$$

$$FWD_t = (FWD_{t-1} + T_{branches,t} \times f_{sb}) \times d_{fwd} \times (1 - f_{burn,fwd,t}) \quad (4.36)$$

$$CWD_t = (CWD_{t-1} + T_{branches,t} \times (1 - f_{sb}) + T_{stem,t}) \times d_{cwd} \times (1 - f_{burn,cwd,t}) \quad (4.37)$$

Whereby *d* is the fraction of the fuel that remains after decomposition:

$$d_i = e^{\frac{-k_i}{tsy}} \quad (4.38)$$

4.3.10 Combustion, heat production and fire emissions

The composition of fire emissions and the produced heat depend on the fuel consumption, the chemical composition of the combusted material, the fuel moisture content and the type of combustion (i.e. complete, flaming or smouldering combustion). In order to represent and quantify those factors in the S4F model, we coupled the estimated fuel moisture and fuel consumption model with a combustion model of chemical reactions during fire as described in Chapter 2 of Rego et al. (2021) (Figure 8). The combustion model requires information about FMC, the chemical composition of the fuel (i.e. fractions of cellulose, lignin and volatiles), about the type of combustion (quantified based on the Equivalent Oxygen to Fuel Ratio, EOFR), air temperature and relative humidity. The combustion model quantifies then the modified combustion efficiency (MCE), the heat yield, and emission factors for H_2O, CO_2, CO, CH_4 and particulate matter (PM). While we directly provide the FMC of leaves, herbaceous vegetation and wood from the previous S4F modules and the SWI for litter, FWD and CWD as input the combustion model, the fractions of cellulose, lignin and volatiles and the EOFR are parametrised for each fuel type based on a sensitivity analysis (Table 6).

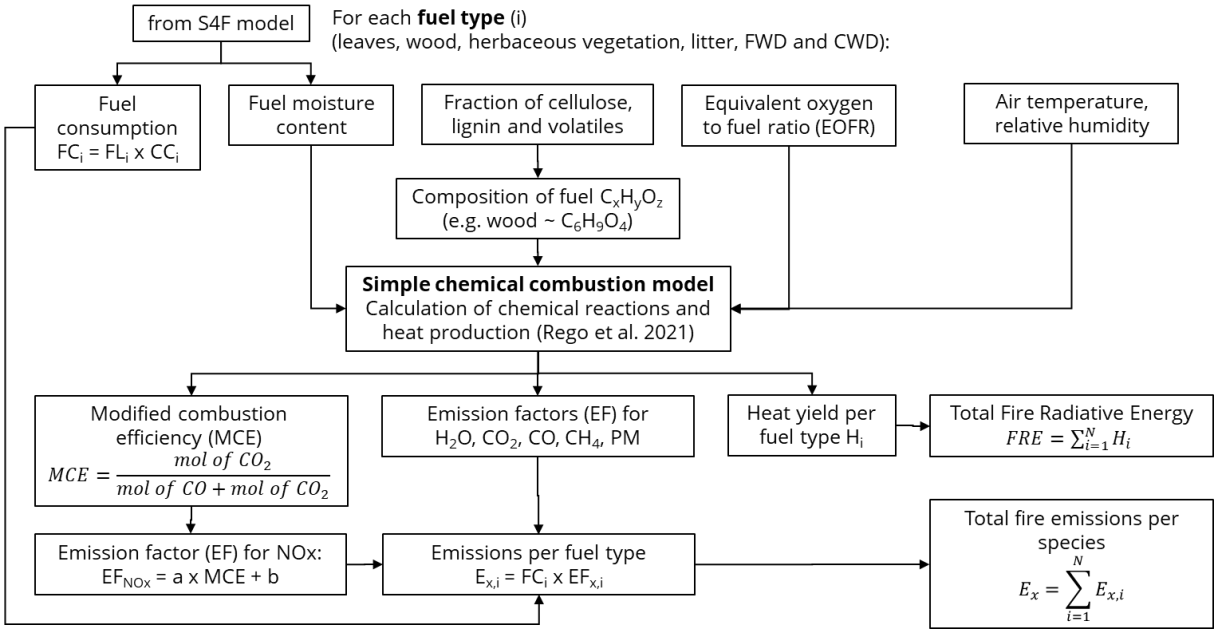

Figure 8: Flowchart about the computation of fire emissions and fire radiative energy in the S4F model using a simple chemical combustion model.

The EOFR is defined as the ratio of oxygen consumed during the actual combustion and the oxygen consumed in complete combustion (Rego et al., 2021). Fires with complete combustion have EOFR = 1, flaming combustion has around EOFR = 0.96 and smouldering combustion has EOFR < 0.9. We took typical values provided by Rego et al. (2021) as EOFR for leaves, wood, herbaceous vegetation, litter, FWD and CWD (Table 6).

The composition of plant biomass in terms of cellulose ($C_6H_{10}O_5$), lignin ($C_{10}H_{12}O_3$), volatiles (e.g. monoterpenes, $C_{10}H_{16}$) and minerals is an important control on the composition of the smoke emissions. The relative composition is known for some plants or fuel types but shows a large variability in nature (e.g. Rego et al., 2021; Waliszewska et al., 2021) but is not available for a large-scale spatial application in a satellite data-driven fire combustion model. Hence we made a couple of assumptions in order to introduce the fractional content of cellulose (f_{ce}) and of volatiles (f_{vo}) in leaves, herbaceous vegetation and wood as calibrate-able model parameters. Specifically, we assume that the fractional content of lignin (f_{li}) in leaves and herbaceous vegetation is:

$$f_{li} = 1 - f_{ce} - f_{vo} - 0.05 \quad (4.39)$$

Which assumes a mineral content of 5%. We assume that the volatiles are monoterpenes ($C_{10}H_{16}$) because most other volatiles have higher carbon contents and hence would cause unrealistic high emission of CO and CH_4, which seems unplausible for the application of the approach at large scales. We treat the fraction of volatiles as a model parameter that we calibrate against observed statistical distributions of emission factors provided by the emission factor database (Andreae, 2019). For wood, we assume a lignin content of:

$$f_{li,wood} = 1 - f_{ce,wood} - 0.01 \quad (4.40)$$

This assumes that wood does not contain volatiles and has a mineral content of 1%. Decaying plant material has a higher content of lignin than cellulose because cellulose decomposes faster. Hence we assume that the fractional content of cellulose in litter, FWD and CWD is only 80% of f_{ce} of leaves and wood, respectively and adjust the fraction of lignin accordingly.

As the production of nitrous oxides (NOx) during fire is highly complex and not considered in the used combustion model, we estimate the emission factor for NOx based on a linear relation with the modified combustion efficiency (MCE):

$$EF_{NOx} = nox_a \times MCE + nox_{b\_} \quad (4.41)$$

Whereby the parameters nox_a and nox_b have been estimated from the data provided in Andreae (2019).

4.3.11 Calibration of model parameters

While some of the parameters of the S4F model (Table 6) can be taken from the literature or from existing databases, other parameters are not well known but can be calibrated from observations. Therefore, we apply an optimisation algorithm to minimise a cost function that quantifies the error between model estimates and observations.

The cost function *J* is defined based on the Kling-Gupta efficiency (Gupta et al., 2009), which accounts for the bias, variance and correlation between model estimates and observations:

$$J_{DS} = \sqrt{\left(\frac{\bar{m}}{\bar{o}} - 1\right)^2 + \left(\frac{\sigma_m}{\sigma_o} - 1\right)^2 + (r-1)^2} \quad (4.42)$$

Whereby r is the correlation coefficient, and $\bar{m}$ and $\bar{o}$ are the mean values and σ_m and σ_o are the standard deviations of the model result and observations, respectively. The cost is defined for each data set *DS*. In a calibration setup with multiple datasets, the total cost is then defined as:

$$J_{total} = \sum_{DS=1}^{N} J_{DS} \quad (4.43)$$

The minimisation of the cost function is achieved by applying the GENOUD algorithm (Mebane and Sekhon, 2011), a genetic optimisation algorithm which also incorporates a local gradient search. The algorithm has been previously used to calibrate parameters of global vegetation models (Forkel et al., 2019a) or to estimate live-fuel moisture content from VOD (Forkel et al., 2023).

The S4F model used in ATBDv2.1 and PVRv2.1 has been calibrated for the Amazon and Southern Africa study regions and for the Siberia test area against the Biomass and Allometry Database, against the GEDI canopy height dataset, above ground woody biomass from ESA CCI, LFMC from the VOD2LFMC dataset, VODCA Ku- and X-VOD, and SMOS L-VOD, and against FRE. Maximum combustion completeness per fuel type has been estimated based on the values from the fuel consumption database (van Wees et al., 2022). Emission factors have been calibrated against the statistical distribution of

emission factors per biome as provided by Andreae et al. (2019). This implies that the computation of tree canopy height, tree biomass components, fuel moisture content, vegetation water content, VOD, fuel consumption, combustion and FRE are constrained by observations. The estimated surface fuel loads (litter, FWD, CWD) have been validated against observational databases. Results of those calibration and validation exercises are included in PVRv2.1.

5 KNMI-S5p: Top-down constraints on fire emissions

Sections 3 and 4 provide a detailed algorithm description of how Sentinel satellite observations of vegetation and surface properties are combined with additional non-satellite (ground-based) information to improve estimates of fire emissions from bottom-up approaches and to better constrain the changing role of vegetation fires in the global carbon cycle. Using Sentinel-5p observations of atmospheric trace gases allows to independently asses these bottom-up emission estimates, thus making best use of the constellation of Sentinel satellites. However, the selected approach for the top-down assessment of bottom-up emissions is strictly speaking not an algorithm, but more of an evaluation/validation activity. Hence, the description of the approach to top-down constrain fire emissions will be provided in the PVR rather than in this ATBD. What follows here is a general outline of possible use of Sentinel-5p type observations for top-down constraining fire emissions and the justification for the approach chosen in Sense4Fire.

5.1 Methods for top-down satellite-based emissions

Over the past two decades several methods have been developed to derive or estimate emissions based on satellite observations of trace gases. In general, three types of emission inversions are discerned: mass balance methods, emission plume modelling, and formal emission inversions (Streets et al., 2013).

Mass-balance methods have long been used, originally for well isolated emission sources (Martin et al., 2006), but more recently expanded to also allow for fitting more complex scenes (Beirle et al., 2019, 2021). Emission plumes vary in space and time due to varying wind speeds and turbulent mixing and dispersion. By taking long term averages, these variations tend to average out as they are generally random. Based on turbulent mixing theory and an average wind direction a spatial probability distribution combined with an average emission source strength can be fitted to the average amount of trace gas over an emission source, resulting in an emission source strength estimate.

Such a mass-balance method has been applied here to constrain seasonal and regional total CO emissions from fires, assuming a long lifetime of the emissions, which implies that the regional excess in burden (and its biases) are linearly depending on regional emissions (and its biases). For this method a dedicated reference (without any regional fire emissions) and baseline (including regional fire emissions) experiments are performed. Then, the evaluation of modelled total trace gas enhancement against

satellite observations (as given in Figure 9) allows for further optimization of the emission estimates on a regional and seasonal scale, by scaling the simulated excess in CO columns due to fire emissions to close the gap with the satellite observations. This scaling is assumed to be needed to optimize the CO emissions.

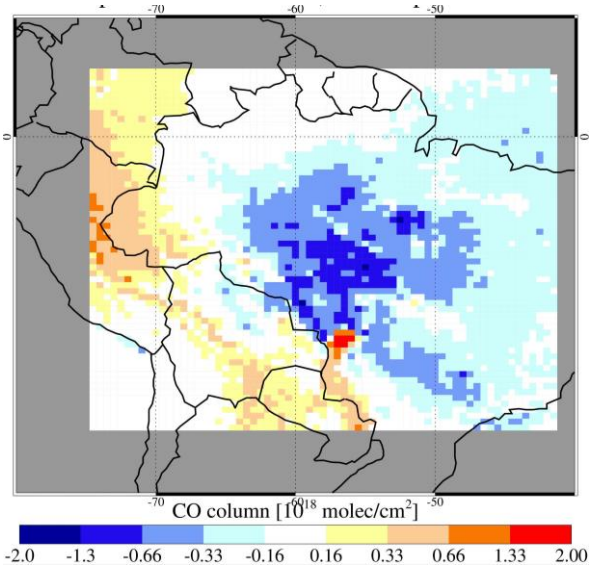

Figure 9: Map of monthly mean CO model bias of and IFS experiment with respect to TROPOMI for September 2020. This bias is directly attributed to fire emissions.

For temporal refinement, i.e. without the need to use long term averaging, emission plumes can also be fitted with relatively simple (Gaussian) emission plume chemistry model simulations. Such simulations take emissions, inner-plume chemistry and plume mixing with ambient air into account, but their representation of plume dispersion is relatively simple (Fioletov et al., 2020; Vermeulen, 2021). Applying such methods works well for satellite observations that are sufficiently accurate to resolve individual emission plumes, which for some satellites and/or trace gas measurements is not achievable. Alternatively, although computationally more expensive, spatially detailed chemistry-transport modelling or even large eddy simulations with atmospheric chemistry could be used for a similar purpose. Fire characterisation and emissions based on Sentinels 1-2-3 as developed within Sense4Fire could serve as a basis for all these types of detailed plume modelling.

An alternative approach to derive fire emissions is based on the assumption that, although models may simulate incorrect trace gas amounts, they are capable of simulating changes in column amounts caused by changes in emissions (Lamsal et al., 2011; Castellanos et al., 2014). By performing a baseline model simulation and a "perturbed emission" simulation, the sensitivity parameter β can be derived as function of space and time that connects changes in column amounts ($\Delta TCNO_2$) to changes in emissions (ΔE):

$$\frac{\Delta E}{E} = \beta \frac{\Delta TCNO_2}{TCNO_2}$$

Then, differences in measured and modelled columns can be converted into differences in emissions relative to the baseline emissions using this β sensitivity parameter (Figure 10) yielding an updated, Sentinel-5p-based emission estimate.

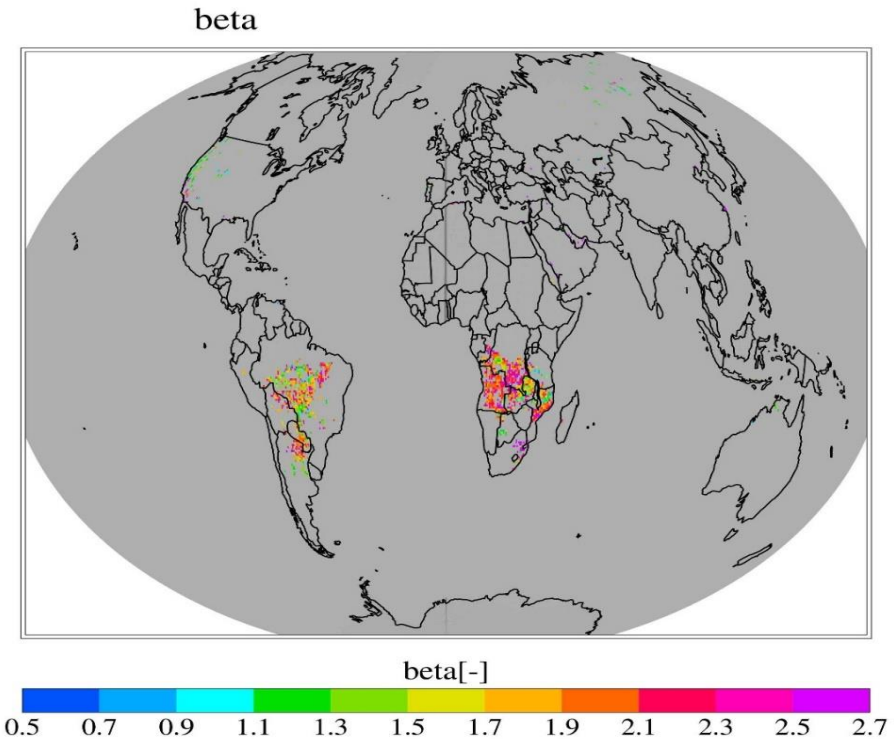

Figure 10: Map of conversion factor β computed from an IFS experiment for August-September 2020, to translate changes in column NO2 to changes in NOX emissions.

Finally, a last category of emission inversions is the more formal data-assimilation based emission inversions. Such methods take full atmospheric chemistry and meteorological conditions like advection, mixing, wet and dry deposition into account. Such methods tend to be computationally expensive, but have the advantage of allowing a more realistic representation of relevant processes while also allowing for missing data (van der A et al., 2017, 2020).

5.2 Suitability of current formal emission inversion methods for fires

These types of methods for determining emissions based on satellite trace gas measurements work well for stationary sources like power plants or industrial complexes, or spatially confined sources such as cities or motorways. This also requires well-defined combustion processes.

However, these methods are less suitable and/or less well-developed for spatio-temporal more variable emission sources. Even changing from a stationary source to one that is moving, such as a ship, already adds a degree of complexity that would require considerable methodological developments.

Natural wildfires are not only variable in time and space, but also depend on fuel characteristics and meteorological conditions, as described in the preceding sections.

Finally, regardless of the particular inversion method, emissions are principally only derived for trace gases that are measured by satellites such as Sentinel-5p. Emission factors that are characteristic of the actual fire type are required to convert the estimated emissions of the measured quantity into those of other trace gases, and/or total carbon. However, this is inevitably associated with additional uncertainties. In theory, it should be possible to incorporate all Sentinel 1-2-3-5p data in a complex emission inversion approach. However, such techniques do not yet exist, thus first requiring dedicated research for developing the most suitable approach and to gain confidence before they could be applied. Such activities fall far outside the scope of the Sense4Fire project.

5.3 Alternative Sentinel-5p approach constraining top-down emissions

Nevertheless, the Sentinel-5p measurements provide unique opportunities to evaluate and constrain fire emissions due to the joint observation of key fire trace gas emissions NO_2 and CO, as well as the unprecedented spatial resolution, accuracy and precision of the Sentinel-5p measurements.

Hence, given the current limitations of emission inversion algorithms to derive fire emissions and to make as much use of the information richness of bottom-up emissions based on Sentinel 1-2-3 satellite observations in combination with Sentinel-5p data, the approach chosen here is to use atmospheric chemistry forward model simulations as an intermediate between the bottom-up emissions and top-down observations of key atmospheric trace gases.

Such an approach can be referred to as a poor-man's inversion method (Huijnen et al., 2016) and essentially relies on an iterative optimisation of model simulations by updating the input emissions, in combination with a detailed uncertainty analysis. Unlike formal emission inversion algorithms, this can rather be considered as a model and bottom-up emission evaluation and verification approach than a formal algorithm. Since such a production evaluation and verification lacks a formal theoretical basis its description is provided in the PVRv2.

6 References

van der A, R. J., Mijling, B., Ding, J., Koukouli, M. E., Liu, F., Li, Q., Mao, H., and Theys, N.: Cleaning up the air: effectiveness of air quality policy for SO_2 and NO_x emissions in China, Atmospheric Chem. Phys., 17, 1775–1789, https://doi.org/10.5194/acp-17-1775-2017, 2017.

van der A, R. J., de Laat, A. T. J., Ding, J., and Eskes, H. J.: Connecting the dots: NOx emissions along a West Siberian natural gas pipeline, Npj Clim. Atmospheric Sci., 3, 1–7, https://doi.org/10.1038/s41612-020-0119-z, 2020.

Abbott, K. N., Leblon, B., Staples, G. C., Maclean, D. A., and Alexander, M. E.: Fire danger monitoring using RADARSAT-1 over northern boreal forests, Int. J. Remote Sens., 28, 1317–1338, https://doi.org/10.1080/01431160600904956, 2007.

Andela, N., Morton, D. C., Giglio, L., Paugam, R., Chen, Y., Hantson, S., Van Der Werf, G. R., and Randerson, J. T.: The Global Fire Atlas of individual fire size, duration, speed and direction, Earth Syst. Sci. Data, 11, 529–552, 2019.

Andela, N., Morton, D. C., Schroeder, W., Chen, Y., Brando, P. M., and Randerson, J. T.: Tracking and classifying Amazon fire events in near real time, Sci. Adv., 8, eabd2713, https://doi.org/10.1126/sciadv.abd2713, 2022.

Andreae, M. O.: Emission of trace gases and aerosols from biomass burning–an updated assessment, Atmospheric Chem. Phys., 19, 8523–8546, 2019.

Andreae, M. O. and Merlet, P.: Emission of trace gases and aerosols from biomass burning, Glob. Biogeochem. Cycles, 15, 955–966, https://doi.org/10.1029/2000GB001382, 2001.

National Institute of Space Research (INPE), PRODES deforestation. http://terrabrasilis.dpi.inpe.br/en/home-page/, accessed March 20, 2020.:

Avitabile, V., Herold, M., Heuvelink, G. B. M., Simon, L., Phillips, O. L., Asner, G. P., Armston, J., Peter, S., Banin, L., Bayol, N., and Berry, N. J.: An integrated pan-tropical biomass map using multiple reference datasets, Glob. Change Biol., 22, 1406–1420, https://doi.org/10.1111/gcb.13139, 2016a.

Avitabile, V., Herold, M., Heuvelink, G. B. M., Lewis, S. L., Phillips, O. L., Asner, G. P., Armston, J., Ashton, P. S., Banin, L., Bayol, N., Berry, N. J., Boeckx, P., Jong, B. H. J., DeVries, B., Girardin, C. A. J., Kearsley, E., Lindsell, J. A., Lopez-Gonzalez, G., Lucas, R., Malhi, Y., Morel, A., Mitchard, E. T. A., Nagy, L., Qie, L., Quinones, M. J., Ryan, C. M., Ferry, S. J. W., Sunderland, T., Laurin, G. V., Gatti, R. C., Valentini, R., Verbeeck, H., Wijaya, A., and Willcock, S.: An integrated pan-tropical biomass map using multiple reference datasets, Glob. Change Biol., https://doi.org/10.1111/gcb.13139, 2016b.

Baccini, A., Goetz, S. J., Walker, W. S., Laporte, N. T., Sun, M., Sulla-Menashe, D., Hackler, J., Beck, P. S. A., Dubayah, R., Friedl, M. A., Samanta, S., and Houghton, R. A.: Estimated carbon dioxide emissions from tropical deforestation improved by carbon-density maps, Nat. Clim. Change, 2, 182–185, https://doi.org/10.1038/nclimate1354, 2012a.

Baccini, A., Goetz, S. J., Walker, W. S., Laporte, N. T., Sun, M., Sulla-Menashe, D., Hackler, J., Beck, P. S. A., Dubayah, R., Friedl, M. A., Samanta, S., and Houghton, R. A.: Estimated carbon dioxide emissions from tropical deforestation improved by carbon-density maps, Nat. Clim. Change, 2, 182–185, https://doi.org/10.1038/nclimate1354, 2012b.

Barrett, K., Baxter, R., Kukavskaya, E., Balzter, H., Shvetsov, E., and Buryak, L.: Postfire recruitment failure in Scots pine forests of southern Siberia, Remote Sens. Environ., 237, 111539, https://doi.org/10.1016/j.rse.2019.111539, 2020.

Bauer-Marschallinger, B., Paulik, C., Hochstöger, S., Mistelbauer, T., Modanesi, S., Ciabatta, L., Massari, C., Brocca, L., and Wagner, W.: Soil Moisture from Fusion of Scatterometer and SAR:

Closing the Scale Gap with Temporal Filtering, Remote Sens., 10, 1030, https://doi.org/10.3390/rs10071030, 2018.

Beirle, S., Borger, C., Dörner, S., Li, A., Hu, Z., Liu, F., Wang, Y., and Wagner, T.: Pinpointing nitrogen oxide emissions from space, Sci. Adv., 5, eaax9800, https://doi.org/10.1126/sciadv.aax9800, 2019.

Beirle, S., Borger, C., Dörner, S., Eskes, H., Kumar, V., de Laat, A., and Wagner, T.: Catalog of NO_x emissions from point sources as derived from the divergence of the NO_2 flux for TROPOMI, Earth Syst. Sci. Data, 13, 2995–3012, https://doi.org/10.5194/essd-13-2995-2021, 2021.

Carvalhais, N., Forkel, M., Khomik, M., Bellarby, J., Jung, M., Migliavacca, M., Mu, M., Saatchi, S., Santoro, M., Thurner, M., Weber, U., Ahrens, B., Beer, C., Cescatti, A., Randerson, J. T., and Reichstein, M.: Global covariation of carbon turnover times with climate in terrestrial ecosystems, Nature, 514, 213–217, https://doi.org/10.1038/nature13731, 2014.

Castellanos, P., Boersma, K. F., and van der Werf, G. R.: Satellite observations indicate substantial spatiotemporal variability in biomass burning NO_x emission factors for South America, Atmospheric Chem. Phys., 14, 3929–3943, https://doi.org/10.5194/acp-14-3929-2014, 2014.

Chuvieco, E., Riaño, D., Aguado, I., and Cocero, D.: Estimation of fuel moisture content from multitemporal analysis of Landsat Thematic Mapper reflectance data: Applications in fire danger assessment, Int. J. Remote Sens., 23, 2145–2162, https://doi.org/10.1080/01431160110069818, 2002.

Cleveland, R. B., Cleveland, W. S., McRae, J. E., and Terpenning, I.: STL: A Seasonal-Trend Decomposition Procedure Based on Loess, J. Off. Stat., 6, 3–73, 1990.

Falster, D. S., Duursma, R. A., Ishihara, M. I., Barneche, D. R., FitzJohn, R. G., Vårhammar, A., Aiba, M., Ando, M., Anten, N., Aspinwall, M. J., Baltzer, J. L., Baraloto, C., Battaglia, M., Battles, J. J., Bond-Lamberty, B., van Breugel, M., Camac, J., Claveau, Y., Coll, L., Dannoura, M., Delagrange, S., Domec, J.-C., Fatemi, F., Feng, W., Gargaglione, V., Goto, Y., Hagihara, A., Hall, J. S., Hamilton, S., Harja, D., Hiura, T., Holdaway, R., Hutley, L. S., Ichie, T., Jokela, E. J., Kantola, A., Kelly, J. W. G., Kenzo, T., King, D., Kloeppel, B. D., Kohyama, T., Komiyama, A., Laclau, J.-P., Lusk, C. H., Maguire, D. A., le Maire, G., Mäkelä, A., Markesteijn, L., Marshall, J., McCulloh, K., Miyata, I., Mokany, K., Mori, S., Myster, R. W., Nagano, M., Naidu, S. L., Nouvellon, Y., O'Grady, A. P., O'Hara, K. L., Ohtsuka, T., Osada, N., Osunkoya, O. O., Peri, P. L., Petritan, A. M., Poorter, L., Portsmuth, A., Potvin, C., Ransijn, J., Reid, D., Ribeiro, S. C., Roberts, S. D., Rodríguez, R., Saldaña-Acosta, A., Santa-Regina, I., Sasa, K., Selaya, N. G., Sillett, S. C., Sterck, F., Takagi, K., Tange, T., Tanouchi, H., Tissue, D., Umehara, T., Utsugi, H., Vadeboncoeur, M. A., Valladares, F., Vanninen, P., Wang, J. R., Wenk, E., Williams, R., de Aquino Ximenes, F., Yamaba, A., Yamada, T., Yamakura, T., Yanai, R. D., and York, R. A.: BAAD: a Biomass And Allometry Database for woody plants, Ecology, 96, 1445–1445, https://doi.org/10.1890/14-1889.1, 2015.

Fan, N., Koirala, S., Reichstein, M., Thurner, M., Avitabile, V., Santoro, M., Ahrens, B., Weber, U., and Carvalhais, N.: Apparent ecosystem carbon turnover time: uncertainties and robust features, Earth Syst. Sci. Data, 12, 2517–2536, https://doi.org/10.5194/essd-12-2517-2020, 2020.

Fioletov, V., McLinden, C. A., Griffin, D., Theys, N., Loyola, D. G., Hedelt, P., Krotkov, N. A., and Li, C.: Anthropogenic and volcanic point source SO_2 emissions derived from TROPOMI on board Sentinel-5 Precursor: first results, Atmospheric Chem. Phys., 20, 5591–5607, https://doi.org/10.5194/acp-20-5591-2020, 2020.

Forkel, M., Dorigo, W., Lasslop, G., Teubner, I., Chuvieco, E., and Thonicke, K.: A data-driven approach to identify controls on global fire activity from satellite and climate observations (SOFIA V1), Geosci. Model Dev., 10, 4443–4476, https://doi.org/10.5194/gmd-10-4443-2017, 2017.

Forkel, M., Drüke, M., Thurner, M., Dorigo, W., Schaphoff, S., Thonicke, K., Bloh, W. von, and Carvalhais, N.: Constraining modelled global vegetation dynamics and carbon turnover using multiple satellite observations, Sci. Rep., 9, 1–12, https://doi.org/10.1038/s41598-019-55187-7, 2019a.

Forkel, M., Dorigo, W., Lasslop, G., Chuvieco, E., Hantson, S., Heil, A., Teubner, I., Thonicke, K., and Harrison, S. P.: Recent global and regional trends in burned area and their compensating environmental controls, Environ. Res. Commun., 1, 051005, https://doi.org/10.1088/2515-7620/ab25d2, 2019b.

Forkel, M., Andela, N., de Laat, J., Huijnen, V., Awotwi, A., de Graaf, M., Kinalczyk, D., Marrs, C., and Wessollek, C.: Sense4Fire PVRv2. Sentinel-based fuel, fire and emissions products to constrain the changing role of vegetation fires in the global carbon cycle. Product Validation Report Version 2., 2022.

Forkel, M., Schmidt, L., Zotta, R.-M., Dorigo, W., and Yebra, M.: Estimating leaf moisture content at global scale from passive microwave satellite observations of vegetation optical depth, Hydrol. Earth Syst. Sci., 27, 39–68, https://doi.org/10.5194/hess-27-39-2023, 2023.

Fuster, B., Sánchez-Zapero, J., Camacho, F., García-Santos, V., Verger, A., Lacaze, R., Weiss, M., Baret, F., and Smets, B.: Quality Assessment of PROBA-V LAI, fAPAR and fCOVER Collection 300 m Products of Copernicus Global Land Service, Remote Sens., 12, 1017, https://doi.org/10.3390/rs12061017, 2020.

Giglio, L., Schroeder, W., and Justice, C. O.: The collection 6 MODIS active fire detection algorithm and fire products, Remote Sens. Environ., 178, 31–41, https://doi.org/10.1016/j.rse.2016.02.054, 2016.

Giglio, L., Boschetti, L., Roy, D. P., Humber, M. L., and Justice, C. O.: The Collection 6 MODIS burned area mapping algorithm and product, Remote Sens. Environ., 217, 72–85, https://doi.org/10.1016/j.rse.2018.08.005, 2018.

Glass, S. and Zelinka, S.: Moisture Relations and Physical Properties of Wood, in: Wood handbook - Wood as an engineering material, U.S. Department of Agriculture, Forest Service, Forest Products Laboratory, Madison, Wisconsin, 2010.

Gupta, H. V., Kling, H., Yilmaz, K. K., and Martinez, G. F.: Decomposition of the mean squared error and NSE performance criteria: Implications for improving hydrological modelling, J. Hydrol., 377, 80–91, https://doi.org/10.1016/j.jhydrol.2009.08.003, 2009.

Hansen, M. C., Potapov, P. V., Moore, R., Hancher, M., Turubanova, S. A., Tyukavina, A., Thau, D., Stehman, S. V., Goetz, S. J., Loveland, T. R., Kommareddy, A., Egorov, A., Chini, L., Justice, C. O., and Townshend, J. R. G.: High-resolution global maps of 21st-century forest cover change, Science, 342, 850–853, https://doi.org/10.1126/science.1244693, 2013.

Harmon, M. E., Fasth, B. G., Yatskov, M., Kastendick, D., Rock, J., and Woodall, C. W.: Release of coarse woody detritus-related carbon: a synthesis across forest biomes, Carbon Balance Manag., 15, 1, https://doi.org/10.1186/s13021-019-0136-6, 2020.

Holland, E. A., Post, W. M., Matthews, E. G., Sulzman, J. M., Staufer, R., and Krankina, O. N.: A Global Database of Litterfall Mass and Litter Pool Carbon and Nutrients, , https://doi.org/10.3334/ORNLDAAC/1244, 2014.

Huijnen, V., Wooster, M. J., Kaiser, J. W., Gaveau, D. L., Flemming, J., Parrington, M., Inness, A., Murdiyarso, D., Main, B., and Van Weele, M.: Fire carbon emissions over maritime southeast Asia in 2015 largest since 1997, Sci. Rep., 6, 26886, 2016.

Jackson, T. J. and Schmugge, T. J.: Vegetation effects on the microwave emission of soils, Remote Sens. Environ., 36, 203–212, https://doi.org/10.1016/0034-4257(91)90057-D, 1991.

Johnson, M. O., Galbraith, D., Gloor, M., De Deurwaerder, H., Guimberteau, M., Rammig, A., Thonicke, K., Verbeeck, H., von Randow, C., Monteagudo, A., Phillips, O. L., Brienen, R. J. W., Feldpausch, T. R., Lopez Gonzalez, G., Fauset, S., Quesada, C. A., Christoffersen, B., Ciais, P., Sampaio, G., Kruijt, B., Meir, P., Moorcroft, P., Zhang, K., Alvarez-Davila, E., Alves de Oliveira, A., Amaral, I., Andrade, A., Aragao, L. E. O. C., Araujo-Murakami, A., Arets, E. J. M. M., Arroyo, L., Aymard, G. A., Baraloto, C., Barroso, J., Bonal, D., Boot, R., Camargo, J., Chave, J., Cogollo, A., Cornejo Valverde, F., Lola da Costa, A. C., Di Fiore, A., Ferreira, L., Higuchi, N., Honorio, E. N., Killeen, T. J., Laurance, S. G., Laurance, W. F., Licona, J., Lovejoy, T., Malhi, Y., Marimon, B., Marimon Junior, B. H., Matos, D. C. L., Mendoza, C., Neill, D. A., Pardo, G., Peña-Claros, M., Pitman, N. C. A., Poorter, L., Prieto, A., Ramirez-Angulo, H., Roopsind, A., Rudas, A., Salomao, R. P., Silveira, M., Stropp, J., ter Steege, H., Terborgh, J., Thomas, R., Toledo, M., Torres-Lezama, A., van der Heijden, G. M. F., Vasquez, R., Guimarães Vieira, I. C., Vilanova, E., Vos, V. A., and Baker, T. R.: Variation in stem mortality rates determines patterns of above-ground biomass in Amazonian forests: implications for dynamic global vegetation models, Glob. Change Biol., 22, 3996–4013, https://doi.org/10.1111/gcb.13315, 2016.

Kaiser, J. W., Heil, A., Andreae, M. O., Benedetti, A., Chubarova, N., Jones, L., Morcrette, J. J., Razinger, M., Schultz, M. G., Suttie, M., and Van Der Werf, G. R.: Biomass burning emissions estimated with a global fire assimilation system based on observed fire radiative power, Biogeosciences, 9, 527–554, https://doi.org/10.5194/bg-9-527-2012, 2012.

Kikuzawa, K., Onoda, Y., Wright, I. J., and Reich, P. B.: Mechanisms underlying global temperature-related patterns in leaf longevity, Glob. Ecol. Biogeogr., 22, 982–993, https://doi.org/10.1111/geb.12042, 2013.

Knorr, W., Kaminski, T., Arneth, A., and Weber, U.: Impact of human population density on fire frequency at the global scale, Biogeosciences, 11, 1085–1102, https://doi.org/10.5194/bg-11-1085-2014, 2014.

Konings, A. G., Rao, K., and Steele-Dunne, S. C.: Macro to micro: microwave remote sensing of plant water content for physiology and ecology, New Phytol., 223, 1166–1172, https://doi.org/10.1111/nph.15808, 2019.

Kuhn-Régnier, A., Voulgarakis, A., Nowack, P., Forkel, M., Prentice, I. C., and Harrison, S. P.: The importance of antecedent vegetation and drought conditions as global drivers of burnt area, Biogeosciences, 18, 3861–3879, https://doi.org/10.5194/bg-18-3861-2021, 2021.

Lamsal, L. N., Martin, R. V., Padmanabhan, A., van Donkelaar, A., Zhang, Q., Sioris, C. E., Chance, K., Kurosu, T. P., and Newchurch, M. J.: Application of satellite observations for timely updates to global anthropogenic NOx emission inventories, Geophys. Res. Lett., 38, https://doi.org/10.1029/2010GL046476, 2011.

Leblon, B., Kasischke, E., Alexander, M., Doyle, M., and Abbott, M.: Fire Danger Monitoring Using ERS-1 SAR Images in the Case of Northern Boreal Forests, Nat. Hazards, 27, 231–255, https://doi.org/10.1023/A:1020375721520, 2002.

van Leeuwen, T. T., van der Werf, G. R., Hoffmann, A. A., Detmers, R. G., Rücker, G., French, N. H. F., Archibald, S., Carvalho Jr., J. A., Cook, G. D., de Groot, W. J., Hély, C., Kasischke, E. S., Kloster, S., McCarty, J. L., Pettinari, M. L., Savadogo, P., Alvarado, E. C., Boschetti, L., Manuri, S., Meyer, C. P., Siegert, F., Trollope, L. A., and Trollope, W. S. W.: Biomass burning fuel consumption rates: a field measurement database, Biogeosciences, 11, 7305–7329, https://doi.org/10.5194/bg-11-7305-2014, 2014.

Li, W., MacBean, N., Ciais, P., Defourny, P., Lamarche, C., Bontemps, S., Houghton, R. A., and Peng, S.: Gross and net land cover changes in the main plant functional types derived from the annual ESA CCI land cover maps (1992–2015), Earth Syst. Sci. Data, 10, 219–234, https://doi.org/10.5194/essd-10-219-2018, 2018.

Lizundia-Loiola, J., Otón, G., Ramo, R., and Chuvieco, E.: A spatio-temporal active-fire clustering approach for global burned area mapping at 250 m from MODIS data, Remote Sens. Environ., 236, 111493, https://doi.org/10.1016/j.rse.2019.111493, 2020.

Makuma-Massa, H., Bemigisha, J., Kyasimire, B., Nyiramahoro, E., Begumana, J., Mugerwa, S., Egeru, A., and Cho, M.: Mapping the Potential for Hay Making in Rangelands: A Methodological Proposition, Rangelands, 39, 152–162, https://doi.org/10.1016/j.rala.2017.07.002, 2017.

Martin, R. V., Sioris, C. E., Chance, K., Ryerson, T. B., Bertram, T. H., Wooldridge, P. J., Cohen, R. C., Neuman, J. A., Swanson, A., and Flocke, F. M.: Evaluation of space-based constraints on global nitrogen oxide emissions with regional aircraft measurements over and downwind of eastern North America, J. Geophys. Res. Atmospheres, 111, https://doi.org/10.1029/2005JD006680, 2006.

Mebane, W. R. and Sekhon, J. S.: Genetic Optimization Using Derivatives: The rgenoud Package for R, J. Stat. Softw., 42, 1–26, https://doi.org/10.18637/jss.v042.i11, 2011.

Moesinger, L., Dorigo, W., Jeu, R. de, Schalie, R. van der, Scanlon, T., Teubner, I., and Forkel, M.: The global long-term microwave Vegetation Optical Depth Climate Archive (VODCA), Earth Syst. Sci. Data, 12, 177–196, https://doi.org/10.5194/essd-12-177-2020, 2020.

Morton, D. C., DeFries, R. S., Nagol, J., Souza, C. M., Kasischke, E. S., Hurtt, G. C., and Dubayah, R.: Mapping canopy damage from understory fires in Amazon forests using annual time series of Landsat and MODIS data, Remote Sens. Environ., 115, 1706–1720, https://doi.org/10.1016/j.rse.2011.03.002, 2011.

Oliva, P. and Schroeder, W.: Assessment of VIIRS 375m active fire detection product for direct burned area mapping, Remote Sens. Environ., 160, 144–155, https://doi.org/10.1016/j.rse.2015.01.010, 2015.

Pedlar, J. H., Pearce, J. L., Venier, L. A., and McKenney, D. W.: Coarse woody debris in relation to disturbance and forest type in boreal Canada, For. Ecol. Manag., 158, 189–194, https://doi.org/10.1016/S0378-1127(00)00711-8, 2002.

Pettinari, M. L. and Chuvieco, E.: Generation of a global fuel data set using the Fuel Characteristic Classification System, Biogeosciences, 13, 2061–2076, https://doi.org/10.5194/bg-13-2061-2016, 2016.

Potapov, P., Li, X., Hernandez-Serna, A., Tyukavina, A., Hansen, M. C., Kommareddy, A., Pickens, A., Turubanova, S., Tang, H., Silva, C. E., Armston, J., Dubayah, R., Blair, J. B., and Hofton, M.: Mapping global forest canopy height through integration of GEDI and Landsat data, Remote Sens. Environ., 253, 112165, https://doi.org/10.1016/j.rse.2020.112165, 2021.

Poulter, B., MacBean, N., Hartley, A., Khlystova, I., Arino, O., Betts, R., Bontemps, S., Boettcher, M., Brockmann, C., Defourny, P., Hagemann, S., Herold, M., Kirches, G., Lamarche, C., Lederer, D., Ottlé, C., Peters, M., and Peylin, P.: Plant functional type classification for earth system models: results from the European Space Agency's Land Cover Climate Change Initiative, Geosci Model Dev, 8, 2315–2328, https://doi.org/10.5194/gmd-8-2315-2015, 2015.

Prichard, S. J., Kennedy, M. C., Andreu, A. G., Eagle, P. C., French, N. H., and Billmire, M.: Next-Generation Biomass Mapping for Regional Emissions and Carbon Inventories: Incorporating Uncertainty in Wildland Fuel Characterization, J. Geophys. Res. Biogeosciences, 124, 3699–3716, https://doi.org/10.1029/2019JG005083, 2019.

Punalekar, S. M., Verhoef, A., Quaife, T. L., Humphries, D., Bermingham, L., and Reynolds, C. K.: Application of Sentinel-2A data for pasture biomass monitoring using a physically based radiative transfer model, Remote Sens. Environ., 218, 207–220, https://doi.org/10.1016/j.rse.2018.09.028, 2018.

Quan, X., Yebra, M., Riaño, D., He, B., Lai, G., and Liu, X.: Global fuel moisture content mapping from MODIS, Int. J. Appl. Earth Obs. Geoinformation, 101, 102354, https://doi.org/10.1016/j.jag.2021.102354, 2021.

Rao, K., Williams, A. P., Flefil, J. F., and Konings, A. G.: SAR-enhanced mapping of live fuel moisture content, Remote Sens. Environ., 245, 111797, https://doi.org/10.1016/j.rse.2020.111797, 2020.

Rego, F. C., Morgan, P., Fernandes, P., and Hoffman, C.: Fire Science: From Chemistry to Landscape Management, Springer International Publishing, Cham, https://doi.org/10.1007/978-3-030-69815-7, 2021.

Reich, P. B., Walters, M. B., Ellsworth, D. S., Vose, J. M., Volin, J. C., Gresham, C., and Bowman, W. D.: Relationships of leaf dark respiration to leaf nitrogen, specific leaf area and leaf life-span: a test across biomes and functional groups, Oecologia, 114, 471–482, https://doi.org/10.1007/s004420050471, 1998.

Roteta, E., Bastarrika, A., Franquesa, M., and Chuvieco, E.: Landsat and Sentinel-2 Based Burned Area Mapping Tools in Google Earth Engine, Remote Sens., 13, 816, https://doi.org/10.3390/rs13040816, 2021.

Saatchi, S. S. and Moghaddam, M.: Estimation of crown and stem water content and biomass of boreal forest using polarimetric SAR imagery, IEEE Trans. Geosci. Remote Sens., 38, 697–709, https://doi.org/10.1109/36.841999, 2000.

Saatchi, S. S., Harris, N. L., Brown, S., Lefsky, M., Mitchard, E. T. A., Salas, W., Zutta, B. R., Buermann, W., Lewis, S. L., Hagen, S., Petrova, S., White, L., Silman, M., and Morel, A.: Benchmark map of forest carbon stocks in tropical regions across three continents, Proc. Natl. Acad. Sci., 108, 9899–9904, https://doi.org/10.1073/pnas.1019576108, 2011a.

Saatchi, S. S., Harris, N. L., Brown, S., Lefsky, M., Mitchard, E. T. A., Salas, W., Zutta, B. R., Buermann, W., Lewis, S. L., Hagen, S., Petrova, S., White, L., Silman, M., and Morel, A.: Benchmark map of forest carbon stocks in tropical regions across three continents, Proc. Natl. Acad. Sci., 108, 9899–9904, https://doi.org/10.1073/pnas.1019576108, 2011b.

Santoro, M., Cartus, O., Carvalhais, N., Rozendaal, D. M. A., Avitabile, V., Araza, A., de Bruin, S., Herold, M., Quegan, S., Rodríguez-Veiga, P., Balzter, H., Carreiras, J., Schepaschenko, D., Korets, M., Shimada, M., Itoh, T., Moreno Martínez, Á., Cavlovic, J., Cazzolla Gatti, R., da Conceição Bispo, P., Dewnath, N., Labrière, N., Liang, J., Lindsell, J., Mitchard, E. T. A., Morel, A., Pacheco Pascagaza, A. M., Ryan, C. M., Slik, F., Vaglio Laurin, G., Verbeeck, H., Wijaya, A., and Willcock, S.: The global forest above-ground biomass pool for 2010 estimated from high-resolution satellite observations, Earth Syst. Sci. Data, 13, 3927–3950, https://doi.org/10.5194/essd-13-3927-2021, 2021.

van der Schalie, R., de Jeu, R. A. M., Kerr, Y. H., Wigneron, J. P., Rodríguez-Fernández, N. J., Al-Yaari, A., Parinussa, R. M., Mecklenburg, S., and Drusch, M.: The merging of radiative transfer based surface soil moisture data from SMOS and AMSR-E, Remote Sens. Environ., 189, 180–193, https://doi.org/10.1016/j.rse.2016.11.026, 2017.

Schroeder, W., Oliva, P., Giglio, L., and Csiszar, I. A.: The New VIIRS 375m active fire detection data product: Algorithm description and initial assessment, Remote Sens. Environ., 143, 85–96, https://doi.org/10.1016/j.rse.2013.12.008, 2014.

Schwieder, M., Buddeberg, M., Kowalski, K., Pfoch, K., Bartsch, J., Bach, H., Pickert, J., and Hostert, P.: Estimating Grassland Parameters from Sentinel-2: A Model Comparison Study, PFG – J. Photogramm. Remote Sens. Geoinformation Sci., 88, 379–390, https://doi.org/10.1007/s41064-020-00120-1, 2020.

Shvetsov, E. G., Kukavskaya, E. A., Buryak, L. V., and Barrett, K.: Assessment of post-fire vegetation recovery in Southern Siberia using remote sensing observations, Environ. Res. Lett., 14, 055001, https://doi.org/10.1088/1748-9326/ab083d, 2019.

Simard, M., Pinto, N., Fisher, J. B., and Baccini, A.: Mapping forest canopy height globally with spaceborne lidar, J. Geophys. Res. Biogeosciences, 116, G04021, https://doi.org/10.1029/2011JG001708, 2011.

Song, X.-P., Hansen, M. C., Stehman, S. V., Potapov, P. V., Tyukavina, A., Vermote, E. F., and Townshend, J. R.: Global land change from 1982 to 2016, Nature, 560, 639–643, https://doi.org/10.1038/s41586-018-0411-9, 2018.

Streets, D. G., Canty, T., Carmichael, G. R., de Foy, B., Dickerson, R. R., Duncan, B. N., Edwards, D. P., Haynes, J. A., Henze, D. K., Houyoux, M. R., Jacob, D. J., Krotkov, N. A., Lamsal, L. N., Liu, Y., Lu, Z., Martin, R. V., Pfister, G. G., Pinder, R. W., Salawitch, R. J., and Wecht, K. J.: Emissions estimation from satellite retrievals: A review of current capability, Atmos. Environ., 77, 1011–1042, https://doi.org/10.1016/j.atmosenv.2013.05.051, 2013.

Sturtevant, B. R., Bissonette, J. A., Long, J. N., and Roberts, D. W.: Coarse Woody Debris as a Function of Age, Stand Structure, and Disturbance in Boreal Newfoundland, Ecol. Appl., 7, 702–712, https://doi.org/10.2307/2269532, 1997.

Thurner, M., Beer, C., Santoro, M., Carvalhais, N., Wutzler, T., Schepaschenko, D., Shvidenko, A., Kompter, E., Ahrens, B., Levick, S. R., and Schmullius, C.: Carbon stock and density of northern boreal and temperate forests, Glob. Ecol. Biogeogr., 23, 297–310, https://doi.org/10.1111/geb.12125, 2014.

Veraverbeke, S., Sedano, F., Hook, S. J., Randerson, J. T., Jin, Y., and Rogers, B. M.: Mapping the daily progression of large wildland fires using MODIS active fire data, Int. J. Wildland Fire, 23, 655–667, https://doi.org/10.1071/wf13015, 2014.

Verger, A. and Descals, A.: Algorithm Theorethical Basis Document: Leaf Area Index (LAI), Fraction of Absorbed Photosynthetically Active Radiation (FAPAR), Fraction of green Vegetation Cover (FCover) Collection 300m Version 1.1, Copernicus Global Land Operations, 2021.

Vermeulen, R.: Using a Bottom-Up Approach to Analyze Individual Ship NO2, MSc thesis, Technical University Eindhoven, 2021.

Vilar, L., Garrido, J., Echavarría, P., Martínez-Vega, J., and Martín, M. P.: Comparative analysis of CORINE and climate change initiative land cover maps in Europe: Implications for wildfire occurrence estimation at regional and local scales, Int. J. Appl. Earth Obs. Geoinformation, 78, 102–117, https://doi.org/10.1016/j.jag.2019.01.019, 2019.

Waliszewska, B., Grzelak, M., Gaweł, E., Spek-Dźwigała, A., Sieradzka, A., and Czekała, W.: Chemical Characteristics of Selected Grass Species from Polish Meadows and Their Potential Utilization for Energy Generation Purposes, Energies, 14, 1669, https://doi.org/10.3390/en14061669, 2021.

Walker, X. J., Rogers, B. M., Veraverbeke, S., Johnstone, J. F., Baltzer, J. L., Barrett, K., Bourgeau-Chavez, L., Day, N. J., de Groot, W. J., Dieleman, C. M., Goetz, S., Hoy, E., Jenkins, L. K., Kane, E. S., Parisien, M.-A., Potter, S., Schuur, E. a. G., Turetsky, M., Whitman, E., and Mack, M. C.: Fuel availability not fire weather controls boreal wildfire severity and carbon emissions, Nat. Clim. Change, 10, 1130–1136, https://doi.org/10.1038/s41558-020-00920-8, 2020.

Wang, L., Quan, X., He, B., Yebra, M., Xing, M., and Liu, X.: Assessment of the Dual Polarimetric Sentinel-1A Data for Forest Fuel Moisture Content Estimation, Remote Sens., 11, 1568, https://doi.org/10.3390/rs11131568, 2019.

van Wees, D., van der Werf, G. R., Randerson, J. T., Rogers, B. M., Chen, Y., Veraverbeke, S., Giglio, L., and Morton, D. C.: Global biomass burning fuel consumption and emissions at 500 m spatial resolution based on the Global Fire Emissions Database (GFED), Geosci. Model Dev., 15, 8411–8437, https://doi.org/10.5194/gmd-15-8411-2022, 2022.

van der Werf, G. R., Randerson, J. T., Giglio, L., Collatz, G. J., Kasibhatla, P. S., and Arellano Jr, A. F.: Interannual variability in global biomass burning emissions from 1997 to 2004, Atmospheric Chem. Phys., 6, 3423–3441, 2006.

van der Werf, G. R., Randerson, J. T., Giglio, L., Collatz, G. J., Mu, M., Kasibhatla, P. S., Morton, D. C., DeFries, R. S., Jin, Y., and van Leeuwen, T. T.: Global fire emissions and the contribution of deforestation, savanna, forest, agricultural, and peat fires (1997–2009), Atmos Chem Phys, 10, 11707–11735, https://doi.org/10.5194/acp-10-11707-2010, 2010.

van der Werf, G. R., Randerson, J. T., Giglio, L., Van Leeuwen, T. T., Chen, Y., Rogers, B. M., Mu, M., Van Marle, M. J., Morton, D. C., Collatz, G. J., and others: Global fire emissions estimates during 1997-2016, Earth Syst. Sci. Data, 9, 697–720, 2017.

Yebra, M., Dennison, P. E., Chuvieco, E., Riaño, D., Zylstra, P., Hunt Jr., E. R., Danson, F. M., Qi, Y., and Jurdao, S.: A global review of remote sensing of live fuel moisture content for fire danger assessment: Moving towards operational products, Remote Sens. Environ., 136, 455–468, https://doi.org/10.1016/j.rse.2013.05.029, 2013.

Yebra, M., Quan, X., Riaño, D., Rozas Larraondo, P., van Dijk, A. I. J. M., and Cary, G. J.: A fuel moisture content and flammability monitoring methodology for continental Australia based on optical remote sensing, Remote Sens. Environ., 212, 260–272, https://doi.org/10.1016/j.rse.2018.04.053, 2018.

Yebra, M., Scortechini, G., Badi, A., Beget, M. E., Boer, M. M., Bradstock, R., Chuvieco, E., Danson, F. M., Dennison, P., Dios, V. R. de, Bella, C. M. D., Forsyth, G., Frost, P., Garcia, M., Hamdi, A., He, B., Jolly, M., Kraaij, T., Martín, M. P., Mouillot, F., Newnham, G., Nolan, R. H., Pellizzaro, G., Qi, Y., Quan, X., Riaño, D., Roberts, D., Sow, M., and Ustin, S.: Globe-LFMC, a global plant water status database for vegetation ecophysiology and wildfire applications, Sci. Data, 6, 1–8, https://doi.org/10.1038/s41597-019-0164-9, 2019.